Transverse Jet Shape Modification in Pb–Pb Collisions at $\sqrt{s_{\mathrm{NN}}} = 2.76$ TeV from Two Particle Correlations

Jussi Viinikainen

Master's thesis
University of Jyväskylä
Department of Physics
Supervisor: Jan Rak
November 8, 2012

Acknowledgements

I would like to thank the ALICE group at the university of Jyväskylä, especially Sami Räsänen and Filip Křížek, for useful discussions and help during the writing of my master's thesis.

Abstract

The medium induced energy losses in heavy ion collisions are generally measured using inclusive particle yields. In this thesis the method of two particle correlations is used to study the possible modifications of the transverse jet shape due to the medium induced energy loss. The main observable in this thesis is the jet fragmentation transverse momentum j_{T}, defined as the transverse momentum component of the jet fragment with respect to the jet axis. This can be measured using leading particle correlations, where the trigger particle approximates the jets axis and the associated particle is identified as the jet fragment.

The pp data at $\sqrt{s} = 2.76$ TeV and Pb–Pb data at $\sqrt{s_{\mathrm{NN}}} = 2.76$ TeV measured by the ALICE experiment are analyzed to study the j_{T} distribution. The track selection criteria, corrections on track reconstruction efficiency and acceptance and centrality class assignments are discussed before constructing the j_{T} distributions. The signal in these distributions is the part coming from the jet fragmentation. The background in pp comes solely from the underlaying event accompanying the hard scattering while in Pb–Pb also the collective flow contributes to it. Two different methods to determine the background component in pp and one in Pb–Pb are presented.

The modifications of transverse jet shapes in Pb–Pb compared to pp are deduced from the comparison of Pb–Pb and pp j_{T} distributions. It is observed that the j_{T} distribution in Pb–Pb is broader (or harder) than that in pp at low momentum region and there is a hint of the j_{T} distribution narrowing (softening) at high momentum region. The low-p_{T} broadening could be possibly associated to the parton multiple scattering and gluon bremsstrahlung inside the medium or to the interference of the longitudinal flow and the fragmentation process. The narrowing of the j_{T} distribution at high-p_{T} could be attributed to the (i) stronger suppression of gluon than quark jets in the nuclear medium or to the (ii) kinematic bias due to the fact that an observed particle of certain transverse momentum corresponds to a harder parton in Pb–Pb collision as it does in pp collision. The harder the parton is, the more collimated the fragmentation gets kinematically.

Tiivistelmä

Energiahäviöitä raskasionitörmäyksissä mitataan yleisesti inklusiivisten hiukkasjakaumien avulla. Tässä tutkielmassa pyritään kaksihiukkaskorrelaatioita käyttäen tutkimaan mahdollisia energiahäviöistä johtuvia jettien poikittaismuotojen muutoksia. Tutkittava suure on jetin poikittaisfragmentaatioliikemäärä j_{T}, joka määritellään jetin fragmentin poikittaisliikemääräkomponenttina jetin akselin suhteen. Tätä voidaan tutkia kaksihiukkaskorrelaatioiden avulla valitsemalla liipaisinhiukkaseksi (trigger particle) suurimman liikemäärän hiukkanen törmäyksessä, jolloin liipaisinhiukkasen liikemäärän voidaan olettaa olevan keskimäärin yhdensuuntainen jetin akselin kanssa. Tällöin liittohiukkanen (associated particle) tulkitaan jetin fragmentiksi.

Työssä analysoidaan ALICE-kokeen mittaamaa dataa pp-törmäyksistä energialla $\sqrt{s} = 2.76$ TeV sekä Pb–Pb-törmäyksistä energialla $\sqrt{s_{\mathrm{NN}}} = 2.76$ TeV. Analyysissa esitellään kriteerit hyväksyttyjen ratojen valinnalle sekä näihin valintoihin liittyvät korjauskertoimet todellisen hiukkasjakauman löytämiseksi. Työssä johdetaan ALICE-kokeen äärellisestä kinemaattisesta alueesta johtuvat korjaukset mitattavien hiukkasparien lukumääriin. Lisäksi esitellään perusidea sentraliteettiluokkien määrittämisestä kokeellisesti. Tämän keskustelun jälkeen rakennetaan j_{T}-jakaumat. Näissä jakaumissa signaali on jetin fragmentaatiosta tuleva osa. Tausta pp-törmäyksissä tulee vain kovaa sirontaa ympäröivästä tapahtumasta, mutta Pb–Pb-törmäyksissä myös kollektiivinen virtaus vaikuttaa taustaan. Taustan määrittämiselle esitetään kaksi erilaista menetelmää pp-tapauksessa ja yksi Pb–Pb-tapauksessa.

Jettien poikittaismuotojen muutoksia Pb–Pb-törmäyksissä verrattuna pp-törmäyksiin etsitään vertaamalla toisiinsa j_{T}-jakaumia Pb–Pb- ja pp-törmäyksissä. Havaitaan, että j_{T}-jakauma Pb–Pb-tapauksessa on leveämpi (kovempi) kuin pp-tapauksessa pienella liikemäärällä ja kapeampi (pehmeämpi) suurella liikemäärällä. Pienellä poikittaisliikemäärällä havaittu j_{T}-jakauman leveneminen voi johtua esimerkiksi perättäisistä siroamisista väliaineessa ja väliaineen indusoimasta gluonisäteilystä tai pitkittäisen kollektiivisen virtauksen interferenssistä jetin fragmentaation kanssa. Mahdollisia syitä suurella poikittaisliikemäärällä havaittuun j_{T}-jakauman kapenemiseen voivat olla (i) gluonijettien kvarkkijettejä suurempi tukahtuminen väliaineessa sekä (ii) eräs kinemaattinen ilmiö. Tietyllä poikittaisliikemäärällä havaitut hiukkaset syntyvät kovemmista alkeishiukkasista Pb–Pb-törmäyksissä kuin ne tekevät pp-törmäyksissä. Mitä kovempi alkeishiukkanen fragmentoituu, sitä voimakkaammin siitä syntyvä jetti on kinemaattisesti kollimoitu.

Contents

Chapter 1

Introduction

Quantum chromodynamics (QCD) is the theory of the strong interaction. It describes interactions between elementary carriers of color charge, quarks and gluons. It is a crucial part of the Standard Model of particle physics, which sums up a lion's share of the current knowledge of the field. Although the basic Lagrangian of QCD is known, certain phenomena are not yet fully understood. One example of these is the confinement of quarks and gluons. In ordinary matter quarks and gluons are confined to colorless hadrons. QCD predicts that at very high temperatures quarks and gluons can deconfine from mother hadrons and propagate freely in a new phase called the quark-gluon plasma (QGP) [1,2]. It is believed that the early universe has undergone through this phase in less than a few microseconds after the Big Bang.

In laboratory, such extreme conditions leading to the creation of QGP are achieved in collisions of ultra-relativistic heavy nuclei. The research facilities achieving the highest energy densities today are the Brookhaven National Laboratory (BNL) at Upton, New York and CERN at Geneva. The Relativistic Heavy Ion Collider (RHIC) at BNL is dedicated to heavy ion physics. It is designed to study collisions of variety of nuclear species ranging from deuteron to gold and uranium nuclei over a broad energy range $\sqrt{s_{\mathrm{NN}}}$ in $7 - 200\,\mathrm{GeV}$. It can also study polarized proton beams up to $\sqrt{s} = 500\,\mathrm{GeV}$. In CERN, on the other hand, the LHC collider is mainly colliding protons to study electroweak physics. However, also heavy nuclei can be accelerated with this machine. Currently the center of mass energy $\sqrt{s_{\mathrm{NN}}} = 2.76$ TeV has been achieved for the Pb–Pb system and the designed energy is $\sqrt{s_{\mathrm{NN}}} = 5.5$ TeV. The difference in energies between RHIC and LHC is rather large and thus LHC opens up a whole new energy regime for heavy ion research.

The main topic of this thesis is to study the properties of QGP using the Pb–Pb data at $\sqrt{s_{\mathrm{NN}}} = 2.76$ TeV measured with the ALICE detector. This is done by studying the modifications of the transverse structure of jets in heavy ion collisions using two particle correlations. To understand the analysis, some basic heavy ion physics concepts and the experimental setup are introduced in Chapter 1. After the introduction, a more detailed description about the analysis is provided in Chapters 2 and 3 before presenting the results in Chapter 4 and conclusions in Chapter 5. Definitions of the used kinematic variables are found from Appendix A.

The unit system used throughout the thesis is the natural unit system where $c = \hbar = k_{\mathrm{B}} = 1$. In this system $[\text{energy}] = [\text{momentum}] = [\text{temperature}] = \frac{1}{[\text{time}]} = \frac{1}{[\text{length}]} = \text{GeV}$ and $\text{GeV} \cdot \text{fm} \approx 5.07$.

1.1 Heavy ion collisions

1.1.1 Quark-gluon plasma

One of the main goals of the heavy ion study is to explore the phase diagram of the strongly interacting matter. The diagram is shown in Fig. 1.1. Ordinary nuclear matter is represented by a black dot at the net baryon density relative to the average nuclear density 1 and at close to zero temperature.

In the ultra-high density and near to zero temperature region the QCD predicts a phase transition into a color superconducting quark matter [3]. This part of the QCD phase diagram is not currently accessible experimentally. On the other hand the ultra-high temperature and near to zero net baryon density QCD phase can be created in ultra-relativistic heavy ion collisions at high energy accelerators. According to the current understanding of the collision trajectory in the QCD phase diagram, the deconfined excited medium is created in the very early stage (< 1 fm) of the collision [4,5]. Later the nuclear matter expands and cools down until it reaches the "freeze-out" stage when the final state particles are formed.

According to lattice calculations, the critical energy density ρ_{c} at which a phase transition from hadron gas to quark-gluon plasma occurs is about $\rho_{\mathrm{c}} \sim 1\,\mathrm{GeV/fm^3}$ [6]. Tab. 1.1 shows approximative energy densities achieved in three different heavy ion accelerators based on a Bjorken estimate [7]. According to these numbers, it is expected that QGP is actually produced in these experiments.

The expectation of the new phase of matter at high temperature and energy density follows from the asymptotic freedom of QCD [2]. This unique feature is a consequence of the fact that QCD is a non-Abelian

Table 1.1: Approximate energy densities achieved in some high energy accelerators estimated using the Bjorken model [7]. The numbers are taken from [8–10]. For comparison, the expected critical energy density ρ_c for QGP transition given by lattice calculations [6] is presented.

Accelerator	Energy density $[\mathrm{GeV/fm^3}]$
LHC	$\gtrsim 16$
RHIC	$\gtrsim 5$
SPS	$\gtrsim 3$
QGP	~ 1

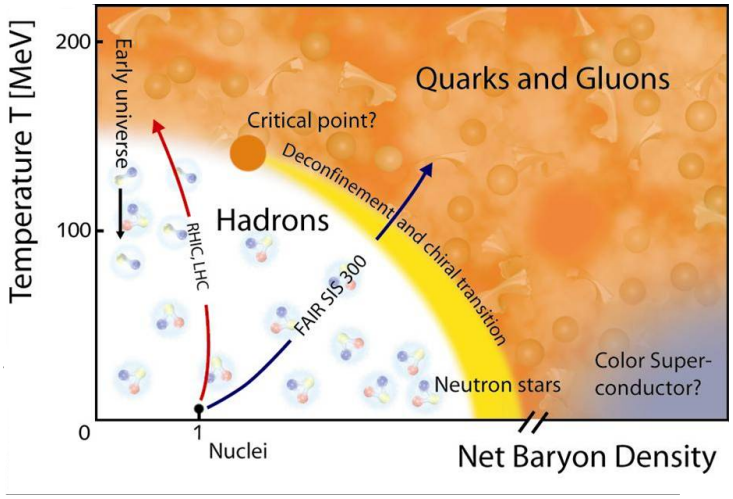

Figure 1.1: The phase diagram of the strongly interacting matter. The density axis is normalized by the density of the ordinary nuclear matter $\rho/\rho_{\mathrm{nuclear}}$. Blue and red arrows reflect the paths probed by different accelerators. The color superconducting phase is predicted theoretically [3], but not yet found experimentally. Figure is taken from [11].

theory. The strong coupling constant α_s is in fact not a constant, but it depends on the energy scale Q^2. At large four-momentum transfer the strength of the coupling diminishes and at low four-momentum transfer it grows. This behavior is explained by the antiscreening phenomenon [12]. To understand antiscreening, it helps to consider the screening phenomenon, that occurs in quantum electrodynamics (QED). The QED vacuum is filled by virtual electron-positron pairs. In the vicinity of a test charge, the vacuum becomes polarized. The virtual particles of opposing charge are attracted to the charge and the virtual particles of like charge are repelled. Hence the virtual fluctuations tend to screen the bare charge. When probing the test charge at smaller distances, the screening is weaker. In QCD, the virtual quark-antiquark pairs produce a similar effect. Besides quark-antiquark pairs, also gluons can form virtual gluon pairs because of their self coupling. Due to the integer spin of the gluons, these virtual gluon pairs produce an effect that is opposite to the screening effect. Now less color charge is seen when going closer to the test charge. It is found that the effect of virtual gluons dominates over the effect of virtual quarks, leading to asymptotic freedom.

1.1.2 The collision geometry

The diameter of a heavy nucleus is nearly macroscopic ($\sim$ 10 fm) and thus the way the nuclei hit each other has a significant impact on the particle production in the collision. To quantify how close the colliding nuclei are to each other, the concept of impact parameter is introduced. The impact parameter $\vec{b}$ is defined as a vector in the transverse plane with respect to the beam connecting the centers of the two colliding nuclei as illustrated by Fig. 1.2.

If the length of the impact parameter is close to 0 in a collision, the nuclei hit each other approximately head on and the collision is called a central collision. If, on the other hand, the length of the impact parameter in a collision is close to $2R$, where R is the radius of the nuclei, the nuclei only slightly scrape each other and the collision is called a peripheral collision. Interesting physics also happens when $|\vec{b}| > 2R$. These collisions are called ultra-peripheral collisions.

Impact parameter also defines special directions in the collision. The plane spanned by the impact parameter and a unit vector in the beam direction is called the reaction plane. An illustration of this is given in Fig. 1.3. Any direction inside the reaction plane is called in-plane direction and the direction perpendicular to the reaction plane is called out-of-plane direction.

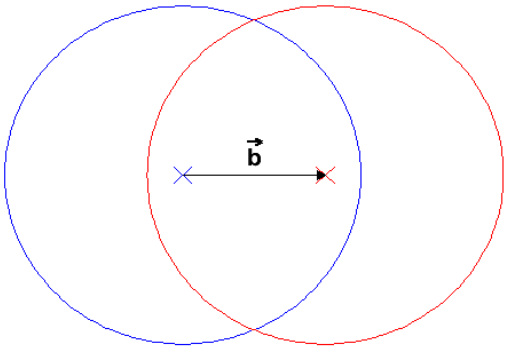

Figure 1.2: A schematic picture of the heavy ion collision in the plane perpendicular to the beam. The centers of the nuclei are marked with crosses. The direction of the impact parameter $\vec{b}$ is called in-plane direction and the direction perpendicular to the impact parameter out-of-plane direction.

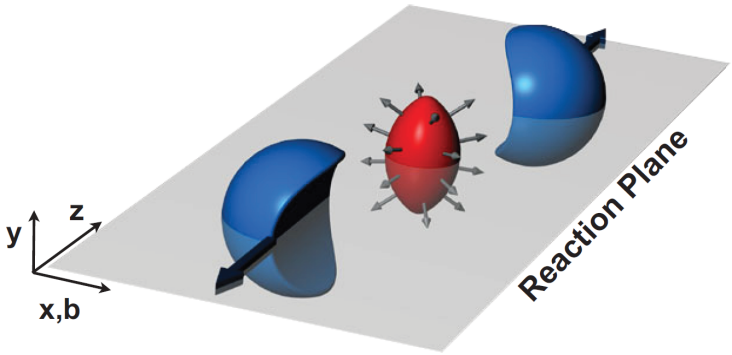

Figure 1.3: A schematic picture of the reaction plane in a situation where the impact parameter coincides with the x-axis. Figure is taken from [13].

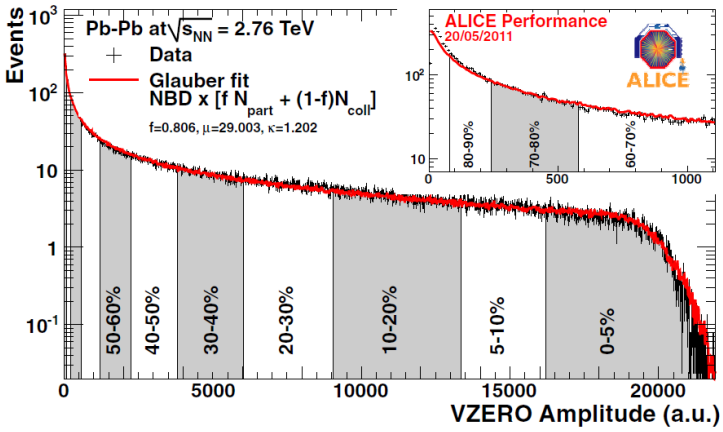

Figure 1.4: A V0 amplitude distribution in the ALICE experiment. The V0 amplitude is proportional to the multiplicity of an event. The distribution is divided into regions of equal area. This division defines the centrality classes in the experiment. Figure is taken from [14].

The nucleons inside the colliding nuclei are divided into two classes, participants and spectators. Participants are the nucleons that take part in the inelastic collisions. In Fig. 1.2 they are roughly the nucleons that are in the area covered by both red and blue nuclei. Spectators are the nucleons that do not take part in the collision. In Fig. 1.2 they are roughly the nucleons, that are outside the overlap zone.

However, the impact parameter cannot be measured experimentally. Instead, information about the collision geometry is classified in terms of collision centrality. To define centrality, an observable that is a monotonic function of the magnitude of the impact parameter is needed. For example, the total number of produced particles (multiplicity) is such an observable. Now the centrality is defined as

$$c(N) = \sum_{n=N}^{\infty} P(n)\,, \tag{1.1}$$

where N is the multiplicity of the collision and $P(n)$ is the probability to have an event where n particles are produced. It can be seen from this definition, that centrality actually gives the fraction of collisions that have at least as large multiplicity as the collision under consideration (see Fig. 1.4). This fraction is usually given as a percentile value. It follows that central collisions with large multiplicity have a centrality value close to 0 % while peripheral collisions have large centrality values. To get better

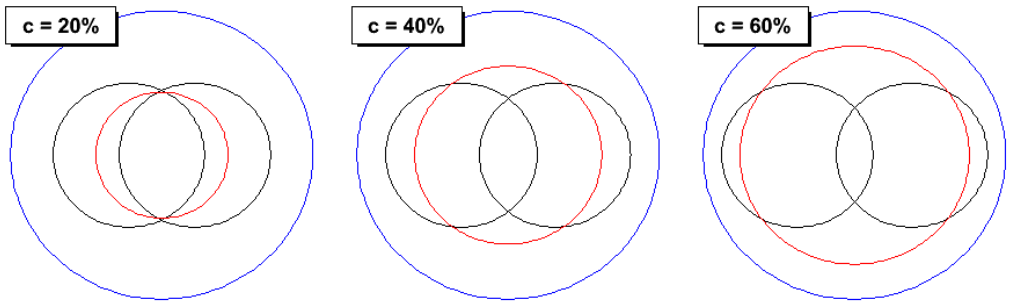

Figure 1.5: A sketch of different centrality classes according to Eq. (1.3). The nuclei (black circles) are shown together with the total cross section (blue circle) and the cross section of the pictured collision (red circle).

geometrical understanding of the centrality, it can be derived starting from Eq. (1.1) (see Appendix B), that centrality actually corresponds to the fraction of the total cross section

$$c(N) = \frac{\sigma_{\text{in}}^{AB}(b(N))}{\sigma_{\text{in}}^{AB}}, \tag{1.2}$$

where σ_{in}^{AB} is the total inelastic nucleus–nucleus cross section and $b(N)$ is the impact parameter for average multiplicity N. If the nuclei are approximated to be hard and black spheres, the total cross section corresponds to the area in which the nuclei can hit each other, which is $\pi(2R)^2$. The cross section for the length of the impact parameter to be less than or equal to b is πb^2. Inserting these approximations to Eq. (1.2) gives a simple geometrical picture of the centrality

$$c = \frac{\pi b^2}{\pi(2R)^2} = \frac{b^2}{4R^2}. \tag{1.3}$$

This simple picture is illustrated in Fig. 1.5.

1.1.3 Collective phenomena and flow

The newly born blob of plasma undergoes a rapid expansion during its short lifetime. The pressure inside the plasma drives this expansion. After a while the energy density dilutes and the plasma hadronizes back to a hadron gas, which later decouples into free streaming hadrons. The timescale of the whole evolution is $\sim 10 - 20\,\text{fm} \approx 10^{-23}\,\text{s}$ [15]. The strong collective motion during the expansion is called the flow.

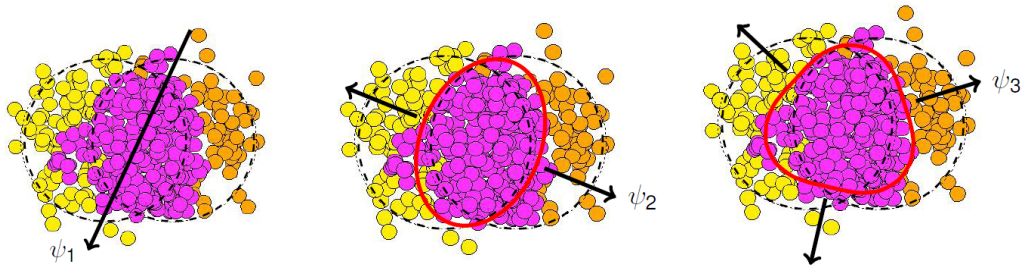

Figure 1.6: A schematic diagram of the simultaneous orientation of directed (ψ_1), elliptic (ψ_2) and triangular (ψ_3) flow. Figure is taken from [16].

Due to the finite size of the heavy nucleus, the initial overlap zone is anisotropic in azimuth (see Fig. 1.2). The larger pressure gradient along the impact parameter leads to a more copious particle production in the in-plane direction as compared to the out-of-plane direction. In other words the hydrodynamical pressure converts the initial spatial anisotropy into a final state momentum anisotropy. The resulting particle distribution is usually described with the help of the Fourier expansion [16]

$$\frac{\mathrm{d}N}{\mathrm{d}\phi}(p_\mathrm{T}) \propto 1 + \sum_{n=1}^{\infty} 2v_n(p_\mathrm{T}) \cos(n(\phi - \psi_n)) \,, \tag{1.4}$$

where $v_n(p_\mathrm{T})$ is the n:th Fourier coefficient, ϕ is the azimuthal angle of the momentum of the outgoing particle and ψ_n is the event plane angle defined by $\langle \sin(n(\phi - \psi_n)) \rangle = 0$. The Fourier coefficients v_n and the angles ψ_n both have a clear physical interpretation, illustrated in Fig. 1.6 for $n = 1, 2, 3$. The coefficients v_n describe the amplitude of a given flow component. Directed flow is reflected by v_1 and it corresponds to the momentum conservation of the colliding system. Elliptic flow is characterized by v_2 and it is related to the almond shape of the collision zone and to pressure gradients. Triangular flow is given by v_3 and it is caused by the initial state fluctuations. The higher coefficients give more complex shapes of the flow, but soon become negligible. The event plane angles ψ_n reflect the orientation of each kind of flow with respect to the chosen reference angle.

It should be noticed that Eq. (1.4) only depends on ϕ, not on η. Indeed, in the measurements the flow is found to be approximately independent of pseudorapidity at least in the region $-2 < \eta < 2$ [17].

1.1.4 Jet quenching models and observables

Jets are collimated streams of hadrons. They are produced in hard scattering processes characterized by large four-momentum transfer Q^2 and color exchange. This is the realm of perturbative quantum chromodynamics (pQCD). In this framework, the hard scattering event is treated as a $2 \rightarrow 2$ process where the two incoming partons collide at center-of-mass energy $\hat{s}$ and the two outgoing partons are emitted back-to-back in the center-of-mass frame. In a proton–proton collision, the parton–parton center-of-mass energy $\hat{s}$ is related to the total proton–proton center-of-mass energy s as $\hat{s} = x_1 x_2 s$, where $x_{1,2}$ correspond to the relative fraction of the proton momentum carried by the partons. The outgoing partons are highly virtual. Partons lose the virtuality by radiating mostly gluons in a process called the parton shower. When the parton reaches a virtuality close to the hadronic scale (~ 1 GeV) the non-perturbative hadronization process begins. The most frequently used hadronization model is the Lund string model [18], where parton pairs are connected to each other with strings. In order to neutralize the color charge, these strings can stretch and break producing new parton pairs with lesser virtuality until only colorless on-shell hadrons remain. The whole process including both showering and hadronization is called the jet fragmentation.

If the parton that initiates the splitting (parent parton) is a quark, the jet is called a quark jet. Similarly a gluon jet is initiated by a gluon. Because of the differences in the splitting functions of quarks and gluons, gluon jets have higher mean multiplicity and wider angular spread than quark jets [19].

Jets provide a good probe for studying the properties of the quark-gluon plasma. The hard scattering takes place very early in the collision and can thus be used to probe the entire history of the collision. Examining how the plasma modifies the jet fragmentation gives information about partonic energy loss mechanisms. Some of the common model frameworks used to describe the energy losses in medium are the Armesto-Salgado-Wiedemann (ASW) formalism [20, 21], the Arnold-Moore-Yaffe (AMY) formalism [22, 23], the Guylassy-Levai-Vitev (GLV) formalism [24, 25] and the higher twist (HT) formalism [26, 27]. All of these models are based on assumptions, that the radiative energy losses dominate over the elastic scatterings inside the medium and that the fragmentation happens outside the medium. In another type of models it is assumed that the showering happens inside the medium. One example of this type of models is YaJEM (Yet another Jet Energy-loss Model) [28, 29], in which the partons gain virtuality when traversing the medium which leads to an increased gluon radiation. An alternative approach is provided by string theory. Here it is

assumed that the correspondence between certain conformal field theories (CFT) and anti de Sitter spaces (AdS) [30–32] can be used to describe the QCD medium in the strong coupling limit. In energy loss calculations the AdS/CFT models are accompanied with a medium induced drag force [29]. The results given by all of the energy loss models are dependent on the chosen medium evolution model. Some of the medium evolution models are presented and the model dependence is illustrated in [33].

The medium induced modifications of jets are studied by comparing the results of the central heavy ion collisions to the results of the proton–proton or proton–heavy ion collisions. These collisions provide a good reference data, since no QGP is produced there.

Nuclear modification factor R_{AA}

Traditionally the energy losses are studied with the help of the nuclear modification factor R_{AA}. It is defined as the ratio of the charged particle yield in nucleus–nucleus collision and the charged particle yield in pp collision scaled by the mean number of binary nucleon–nucleon collisions [34]:

$$R_{\mathrm{AA}}(p_{\mathrm{T}}) = \frac{\left(1/N_{\mathrm{evt}}^{\mathrm{AA}}\right) \mathrm{d}^2 N_{\mathrm{ch}}^{\mathrm{AA}}/\mathrm{d}\eta \mathrm{d}p_{\mathrm{T}}}{\langle N_{\mathrm{coll}} \rangle \left(1/N_{\mathrm{evt}}^{\mathrm{pp}}\right) \mathrm{d}^2 N_{\mathrm{ch}}^{\mathrm{pp}}/\mathrm{d}\eta \mathrm{d}p_{\mathrm{T}}} \,. \tag{1.5}$$

Even though the general suppression of the yield of high-p_{T} particles in heavy ion collisions can be seen from the data [34], R_{AA} provides only limited information about the actual mechanisms of the energy losses. In [35], several simple toy models are constructed by assigning different averaged energy loss probability distributions to them. It is seen, that all of these models can be tuned to fit the RHIC R_{AA} data (see the left panel of Fig. 1.7). For the details on how the energy losses are implemented in the used toy models, see [35].

The limited ability of R_{AA} to seperate valid energy loss models from flawed ones (discriminating power) can be improved by fitting many observables simultaneously [36]. For this, more differential observables are needed.

The ratio of per trigger associated yields I_{AA}

One of the more differential observables that can improve the capability to separate the energy loss models is the ratio of per trigger associated yields I_{AA}. It is defined in the framework of two particle correlations (for two particle correlations, see Section 2.1) to be the ratio of the per trigger

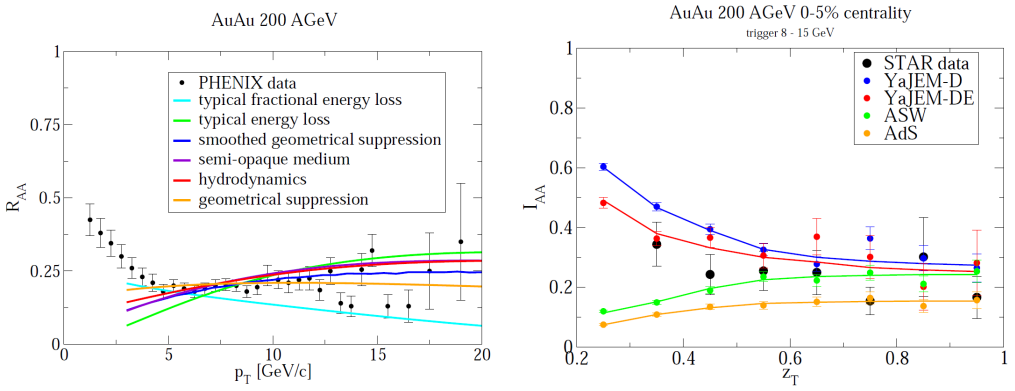

Figure 1.7: *Left*: Different toy model predictions (colored lines) drawn together with the PHENIX R_{AA} data (black points) for π^0 at 0–10 % centrality bin. Figure is taken from [35]. *Right*: Different model predictions (colored points) drawn together with the STAR I_{AA} data (black points). The data is plotted as a function of $z_{\mathrm{T}} = \frac{p_{\mathrm{Ta}}}{p_{\mathrm{Tt}}}$, where p_{Tt} is the trigger particle transverse momentum and p_{Ta} the associated particle transverse momentum. Figure is taken from [36].

normalized yields of associated particles coming from jet fragmentation in heavy ion (Y_{AA}) and proton–proton (Y_{pp}) collisions

$$I_{\mathrm{AA}} = \frac{\frac{1}{N^{\mathrm{AA}}_{\mathrm{trigg}}} Y_{\mathrm{AA}}}{\frac{1}{N^{\mathrm{pp}}_{\mathrm{trigg}}} Y_{\mathrm{pp}}} . \tag{1.6}$$

When the yields are defined this way, the observable is more sensitive to the jet physics. The discriminating power for different energy loss mechanisms is improved, as can be seen in Fig. 1.7. Below $z_{\mathrm{T}} = p_{\mathrm{Ta}}/p_{\mathrm{Tt}} = 0.5$ the theory curves for ASW [20,21] and AdS [30–32] models show different trend than those for YaJEM models [28,29]. In [36] this difference is explained by the contribution of subleading shower partons to the distribution. ASW and AdS do not track these partons, but YaJEM models take care of them. However, it is also noted in [36] that the hydrodynamical model for the medium can be chosen also in such a way, that YaJEM models do not fit the data and the others do.

The motivation for this thesis is to further generalize I_{AA} and to construct an observable that is sensitive to the jet shape. This new observable is then used to study the pp data at $\sqrt{s} = 2.76$ TeV and Pb–Pb data at $\sqrt{s_{\mathrm{NN}}} = 2.76$ TeV measured by the ALICE experiment.

1.2 The ALICE experiment

ALICE (A Large Ion Collider Experiment) is a dedicated heavy ion experiment at LHC. The prime aim of the experiment is to study in detail the behavior of matter at high densities and temperatures. The main characteristics in the design of ALICE are excellent tracking and particle identification in the environment of large particle density.

A schema of the ALICE detector can be seen in Fig. 1.8. The most important detectors for the tracking surround the interaction vertex in the midrapidity covering full azimuth. The Inner Tracking System (ITS) is the closest detector to the interaction vertex. It consists of six layers of silicon detectors and its main purpose is to locate the primary vertex and secondary decay vertices and to provide accurate tracking for low momentum particles [37]. ITS is surrounded by the Time Projection Chamber (TPC), which does a 3D scan of the charged particle track profiles based on the ionization trace they leave in the gas chamber of the detector [38]. This information can be used to determine the momentum of the particles and to identify the particles. After TPC, there is the Transition Radiation Detector (TRD). This detector provides accurate electron identification as it is able to distinguish electrons from charged pions [39]. The Time Of Flight detector (TOF) provides more charged particle identification [40]. To make the particle identification as complete as possible, the High Momentum Particle Identification Detector (HMPID), which is a Cherenkov radiation based detector, is placed to the next layer [41].

The electromagnetic calorimeters are situated in the next layer of detectors. A detector called the Electromagnetic Calorimeter (EMCal) is used for jet and photon triggering and measurement [42]. There is also another electromagnetic calorimeter, called the Photon Spectrometer (PHOS). This detector can make measurements of photons and charged particles with high energy and position resolution [43]. The difference between these two is, that EMCal has larger acceptance, but PHOS has better energy resolution.

A solenoid magnet surrounds the central detectors. With the produced homogeneous magnetic field of 0.5 T ALICE can reconstruct tracks whose p_{T} is between 0.15 GeV and 100 GeV. On the top of the magnet there is the ALICE Cosmic Ray Detector (ACORDE). This is used as a cosmic ray trigger for calibrations and also for studying cosmic rays [44].

Another important set of detectors are the forward detectors, since they provide event characteristics and triggering. Next to ITS, there are V0 and T0 detectors. The main purpose of T0 is to provide precise timing signals for triggering and time of flight measurements [45]. V0 can provide

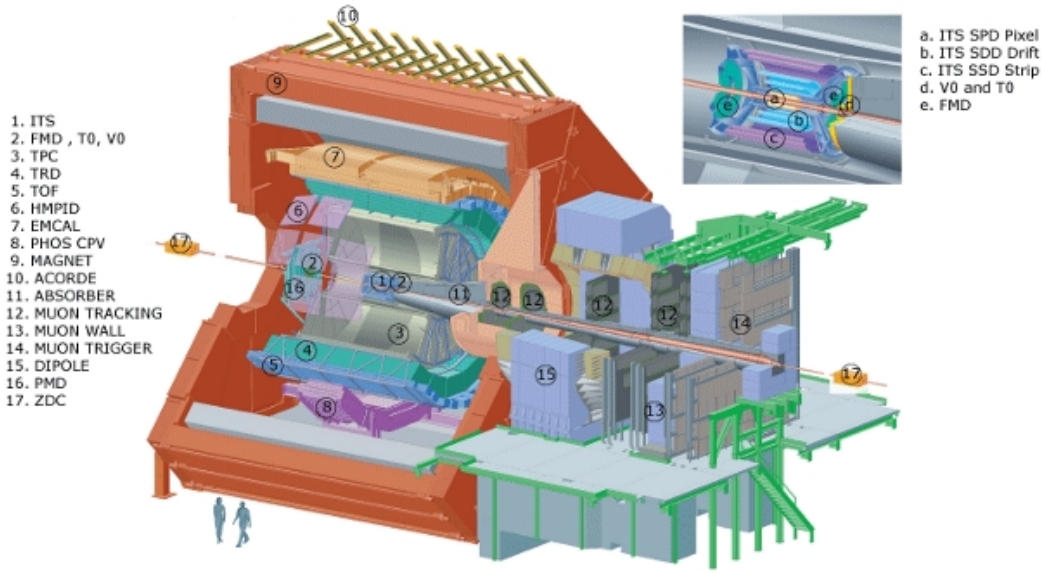

Figure 1.8: The ALICE detector. The different parts of the detector provide: tracking and particle identification (1,3-6), electromagnetic calorimetry (7-8), magnetic field (9), cosmic ray detection (10), forward rapidity detection (2,16-17) and muon detection (11-15).

centrality triggers and multiplicity information [45]. Both of them are also used as luminometers. The Forward Multiplicity Detector (FMD), also situated close to ITS, is used to measure multiplicities in the forward direction [45, 46].

A bit farther away, the Photon Multiplicity Detector (PMD) measures the photon multiplicities and their spatial distributions [47]. Far away from the other detectors, just next to the beam pipe, there are the Zero Degree Calorimeters (ZDC), which provide a centrality trigger of the collision [48]. The only hadronic calorimeters in the ALICE experiment are found from here.

The muon detection system is located in the forward direction. After hadrons and photons are stopped by the absorber, the tracks of the muons are measured by determining their positions before and after the dipole magnet blocks [49]. Next the muon wall filters away low energy muons and lets only high energy muons to get to the trigger to provide a trigger signal. This muon detection system allows the study of heavy quarkonia and other vector mesons that decay through the muonic decay channels.

Chapter 2

Analysis concept

2.1 Two particle correlations

In triggered two particle correlations, the particles in the event are divided into three categories, trigger particles, associated particles and other particles. Trigger particles and associated particles have to meet the preset requirements for them. These are usually defined to be certain transverse momentum intervals. The other particles that do not meet these requirements are disregarded in the analysis. After the trigger particles and the associated particles are found, all possible trigger-associated pairs among them are formed. From these pairs, the sought quantity is measured (for example $\Delta\phi = \phi_t - \phi_a$ or $\Delta\eta = \eta_t - \eta_a$). The correlations between the trigger and the associated particles are searched statistically.

A special case is the leading particle correlation. Here the trigger particle is chosen to be the particle with the highest transverse momentum in the collision. Leading particle correlations are very well suitable for studying jets since the leading particle with high-p_T approximates the jet axis.

Pairs with $|\Delta\phi| < \pi/2$ fill the so called near side region and pairs with larger difference in the azimuthal angle are said to be in the away side. These regions are illustrated by Fig. 2.1. The particles that form the correlation peak in the near side come from the same parton fragmentation process as the trigger particle. The particles in the away side correlation peak come from the same hard scattering but different parton as the trigger. The combinatoric background arises when the trigger is paired with particles from the underlaying event.

Another method for the jet studies is the full jet reconstruction, where a jet finding algorithm is applied to the data to identify the jet. Both of these approaches have their advantages and disadvantages. Jet reconstruction

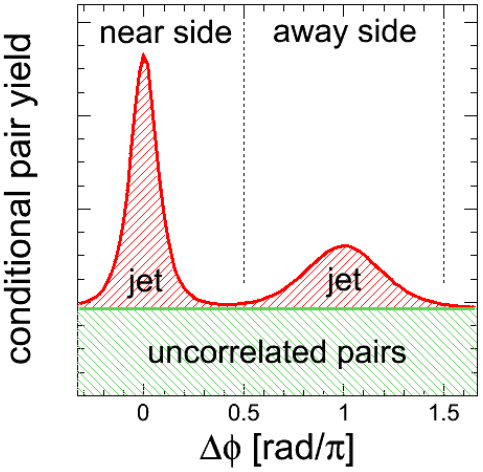

Figure 2.1: Example of the azimuthal correlation function in a pp collision. The two jet peaks are standing at $^{\Delta\phi}/_{\pi} = 0$ and $^{\Delta\phi}/_{\pi} = 1$ above the combinatoric background.

gives event-by-event kinematics, but from di-hadron correlations only the average jet kinematics are obtained. Also the results from the full jet reconstruction are more easily related to the partons that are initiating the jet. However, the di-hadron correlations can be used to study jets with lower p_{T} because of the statistical approach. The two particle correlation method is also easier to handle experimentally. There are large background fluctuations in the heavy ion environment, so it is difficult to define the jet correctly in the full jet reconstruction. Also in general the jet observables have dependence on the chosen jet reconstruction algorithm.

2.2 Jet shapes

The main goal of this thesis is to study the near side transverse jet shapes in the framework of two particle correlations. By comparing near side peak profiles in heavy ion and proton–proton collisions, the influence of the medium on the parton fragmentation can be studied.

In this thesis, the following jet shape modification scenarios are considered: broadening, narrowing and no modification. Broadening of the jet shape is suggested with models that take into account multiple scatterings and radiative energy losses of the jet fragments inside the QGP [50]. Some authors also expect that the interference of the collective longitudinal flow

with jet fragmentation causes broadening of the jet cone [51].

There are some effects, like gluon filtering [52], that might narrow the jets in heavy ion collisions. Quark jets are known to be narrower than gluon jets [19]. Because gluons couple more strongly to the medium than quarks do, gluons are absorbed by the medium more readily than quarks. Hence it is more likely that the parent parton for a jet in medium is a quark and thus it is more likely to have a narrower jet. Another explanation for the possible jet narrowing is a kinematic bias. The fragmentation variable $z = p_T^{\text{hadron}}/p_T^{\text{parton}}$ tells the fraction of the original parton transverse momentum taken by the observed hadron. For a 10 GeV trigger hadron, the expected z values at LHC energies are $\langle z^{vac} \rangle \approx 0.5$ for a fragmentation in vacuum and $\langle z^{med} \rangle \approx 0.3$ for a fragmentation in medium [52]. Hence a 10 GeV trigger corresponds to a $\sim$ 20 GeV parton in vacuum but to a $\sim$ 33 GeV parton in medium. Kinematically harder partons have narrower fragmentation than softer ones, so this effect causes jets with similar trigger momenta look narrower in heavy ion collisions compared to pp collisions.

In case that there is a strong surface bias [52] and the jet fragments outside the medium it is possible that no significant modifications of the jet shape are seen.

2.3 Jet fragmentation transverse momentum j_T

The main observable in this study is the jet transverse fragmentation momentum j_T, which is defined as the transverse momentum component of the jet fragment with respect to the jet axis. This can be connected to the two particle correlations by requiring that the trigger particle is a leading particle with high-p_T. In this case it can be assumed, that the trigger particle momentum approximates the jet axis. Identifying the associated particle as the jet fragment allows to write j_T as the transverse momentum component of the associated particle momentum $\vec{p}_a$ with respect to the trigger particle momentum $\vec{p}_t$:

$$j_T = \frac{|\vec{p}_t \times \vec{p}_a|}{|\vec{p}_t|}. \tag{2.1}$$

The longitudinal component of $\vec{p}_a$ with respect to $\vec{p}_t$ is called $\vec{k}_{\parallel}$ and its magnitude is:

$$k_{\parallel} = \frac{\vec{p}_t \cdot \vec{p}_a}{|\vec{p}_t|}. \tag{2.2}$$

Fig. 2.2 illustrates these definitions graphically.

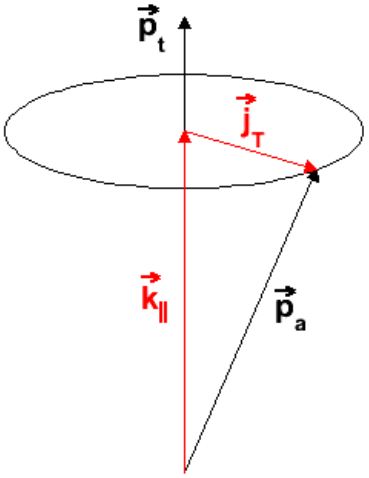

Figure 2.2: Illustration of $\vec{j}_T$ and $\vec{k}_{||}$. When the trigger particle is a leading particle that approximates the jet axis sufficiently well, the $\vec{j}_T$ can be written as the transverse momentum component of the associated particle momentum $\vec{p}_a$ with respect to the trigger particle momentum $\vec{p}_t$. The vector $\vec{k}_{||}$ is the longitudinal component of $\vec{p}_a$ with respect to $\vec{p}_t$.

The first jet transverse fragmentation momentum measurements were done by the CCOR collaboration at ISR (Intersecting Storage Rings) [53]. Later the root-mean-square $\sqrt{\langle j_T^2 \rangle}$ values for different transverse momenta were determined for example by the PHENIX collaboration at RHIC [54] before the first number distributions as a function of j_T were measured by the CDF collaboration at Tevatron for $p\bar{p}$ collisions [55]. Recently the ATLAS collaboration at LHC has published these results for heavy ions using the method of full jet reconstruction [56]. No significant modification in the transverse jet shapes is reported there (see Fig. 2.3). In this thesis the jet fragmentation is studied using different analysis techniques.

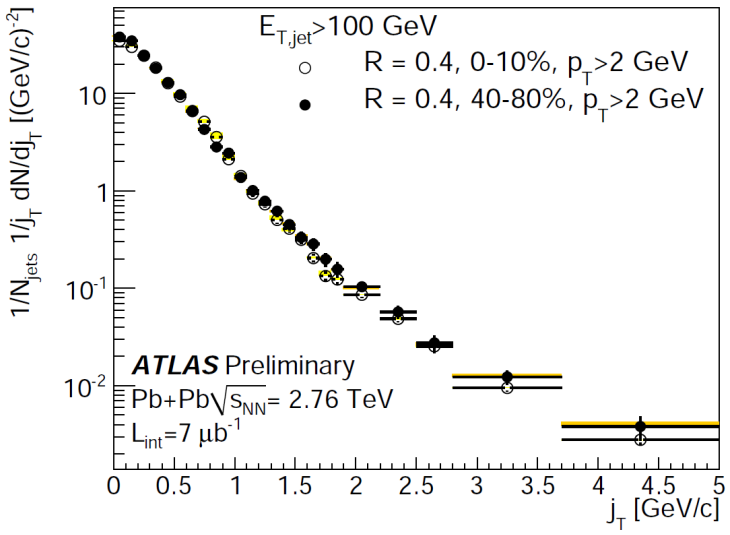

Figure 2.3: The distribution of the jet fragmentation transverse momentum (j_T) measured by the ATLAS collaboration for central and peripheral Pb–Pb data at $\sqrt{s_{NN}} = 2.76$ TeV. The yellow and orange bands show the systematic uncertainties from the subtraction of the underlying event contribution. Figure is taken from [56].

Chapter 3

Data analysis

The analysis aims to study the j_T distributions from the near side jet fragmentation. The measured j_T distribution contains contributions from the jet fragmentation (signal) and the underlaying event (background). The goal is to extract the signal from the measured distribution.

In this thesis 15 million events of Pb–Pb data (taken in 2010) and 55 million events of pp data (taken in 2011) taken by ALICE are analyzed.

3.1 Track cuts

The criteria used in the track selection are listed in Tab. 3.1. These cuts aim to select the charged physical primary tracks that come from the event vertex and to suppress the secondary tracks coming from decays and fake track matchings. Primary particles are all particles produced in the collision, including products of strong and electromagnetic decays as well as weak decays of charmed and bottom particles, but excluding feed-down products from strange weak decays and other secondary particles. The secondary particles are for example γ-conversions and products from secondary hadronic interactions with the detector material [57].

The z vertex cut $|z_{\text{vertex}}| < 10$ cm selects the reaction vertices, where z position can be at most 10 centimeters away from the center of the detector in the beam direction. Combined with the pseudorapidity cut $|\eta| < 0.8$, these two cuts select the region where ALICE tracking detectors have nearly uniform reconstruction efficiency and acceptance.

Primary tracks are effectively selected by the cut on the distance of their closest approach (DCA) to the reconstructed vertex. The position of the vertex is determined by a sophisticated minimizing algorithm. Only tracks that are closer to the vertex than the DCA value are accepted.

Table 3.1: Track quality cuts used in this analysis. See the text for details.

Accepted pseudorapidity range	$\lvert\eta\rvert < 0.8$
Accepted z vertex range	in pp -10 cm $< z_{\text{vertex}} < 10$ cm in Pb–Pb -8 cm $< z_{\text{vertex}} < 8$ cm
Maximal DCA to vertex in XY	$0.0182\text{ cm} + 0.0350\text{ cm} \left(\frac{p_{\text{T}}}{\text{GeV}}\right)^{-1.01}$
Maximal DCA to vertex in Z	2 cm
Minimal number of TPC clusters	70
Maximal χ^2 per one TPC cluster	4
Do not accept kink daughters	
Require TPC refit	
Require ITS refit	

In some cases a kink on otherwise smooth track can be found. The kink indicates a place where the original mother particle decayed to a charged daughter particle. The kink daughter cut removes a significant portion of these secondary tracks.

The number of required clusters in the time projection chamber (TPC) and the maximum χ^2 per one TPC cluster are related to the quality of the track inside TPC, which is the most accurate tracking device of ALICE. If the required amount of clusters get a tracking signal and the χ^2 value is low enough, the track is considered to be good enough that accurate measurements can be made. In ALICE TPC the maximum number of clusters a track can have is 159.

Last in the list are TPC and inner tracking system (ITS) refits. These are done to find the track parameters at the vertex and to improve the global track parameters [58].

3.2 Track efficiency

When analyzing the data, it has to be taken into account that the detectors are not perfect. There may be situations where some primary particle tracks are missed completely and then there could also be situations where some fake tracks, that do not correspond to any true particle, are constructed. Another issue that affects the tracking efficiency besides detecting the particles is selecting the primary particles from the detected particles. The track cuts are tuned to select the tracks that have high probability to be created by primary particles, but they have only limited efficiency.

These effects are studied with Monte Carlo simulations. The simulations have to be detector system specific. For this analysis the proton–proton events are simulated with the PYTHIA Monte Carlo event generator and embedded to the GEANT3 framework to study the detector response [59]. The HIJING event generator is used for the heavy ion track efficiency study. The correction factors for the reconstruction efficiency and the contamination of the reconstructed sample of primary tracks are calculated from the simulations.

The reconstruction efficiency C_{Eff} gives the probability that a primary track is reconstructed . This is given by the equation

$$C_{\mathrm{Eff}} = \frac{N_{\mathrm{rec\,primary}}}{N_{\mathrm{primary}}}\,, \tag{3.1}$$

where $N_{\mathrm{rec\,primary}}$ is the number of the reconstructed charged primary tracks in the required pseudorapidity window in the simulation and N_{primary} the number of all charged primary tracks produced in the simulation in the same pseudorapidity window.

The purity P gives the fraction of properly selected primary tracks among all the reconstructed tracks.

$$P = \frac{N_{\mathrm{rec\,primary}}}{N_{\mathrm{rec}}}\,, \tag{3.2}$$

where N_{rec} is the number of all reconstructed charged tracks in the chosen pseudorapidity window.

In an experiment N_{rec} tracks are reconstructed. Reconstructed tracks include true and fake physical primaries. The original number of physical primaries can be obtained from Equations (3.1) and (3.2):

$$PN_{\mathrm{rec}} = C_{\mathrm{Eff}} N_{\mathrm{primary}} \Rightarrow N_{\mathrm{primary}} = \frac{P}{C_{\mathrm{Eff}}} N_{\mathrm{rec}}\,. \tag{3.3}$$

From here, the total correction factor $C(p_{\mathrm{T}})$ is defined to be

$$C(p_{\mathrm{T}}) = \frac{N_{\mathrm{primary}}}{N_{\mathrm{rec}}} = \frac{P}{C_{\mathrm{Eff}}}\,. \tag{3.4}$$

Purity P, reconstruction efficiency C_{Eff} and the total correction factor $C(p_{\mathrm{T}})$ are obtained from the Monte Carlo simulation as a function of the transverse momentum p_{T}. Examples of these are shown in Fig. 3.1. In the case of two particle correlations the corrections for the trigger and the associated particle are assumed to be independent. Thus the same

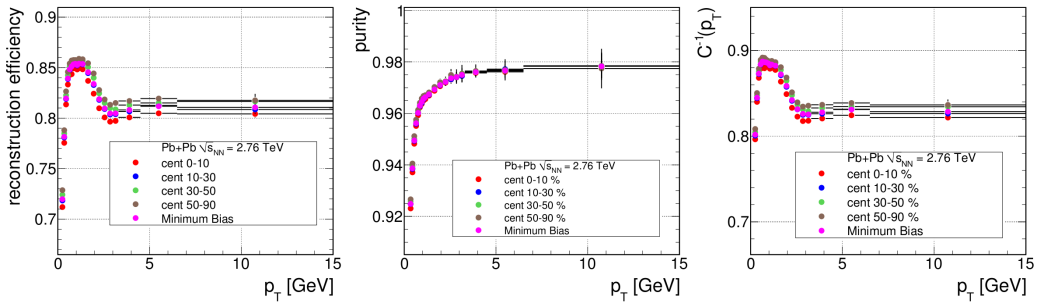

Figure 3.1: The functions for reconstruction efficiency C_{Eff}, purity P and the inverse of the total correction factor $C(p_{\mathrm{T}})$ given by a Monte Carlo simulation for Pb–Pb data at $\sqrt{s_{\mathrm{NN}}} = 2.76$ TeV [59].

total correction function can be used separately for both of the particles to obtain total correction factors $C(p_{\mathrm{Tt}})$ and $C(p_{\mathrm{Ta}})$. The total pair correction factor $C_{\mathrm{pair}}(p_{\mathrm{Tt}}, p_{\mathrm{Ta}})$ is then calculated as

$$C_{\mathrm{pair}}(p_{\mathrm{Tt}}, p_{\mathrm{Ta}}) = C(p_{\mathrm{Tt}})C(p_{\mathrm{Ta}})\,. \tag{3.5}$$

3.3 Pseudorapidity acceptance

The restricted pseudorapidity coverage leads to a need to make acceptance corrections to the data, since it is more likely to see a particle pair with small $\Delta\eta$ compared to a pair with large $\Delta\eta$. This situation is illustrated in Fig. 3.2.

The pair acceptance correction can be derived with the help of Fig. 3.2. The line segment l_0 shows the possible (η_1, η_2) values for $\Delta\eta = \eta_1 - \eta_2 = 0$. This line segment is longer than segments l_1 and l_{-1}, which correspond to the possible values for some fixed $\Delta\eta > 0$ and $\Delta\eta < 0$, respectively. It is assumed, that both of the particles have uniform pseudorapidity distributions. This means that it is equally likely to get any η value for η_1 and η_2. Thus the length of the line segment is directly proportional to the probability to see the particle pair with a given pseudorapidity gap.

The length of the line segment can be obtained for example from the right triangle it forms with the limits of the pseudorapidity window. It can be read from Fig. 3.2 that the length for both of the legs are $2\eta_{\mathrm{max}} - |\Delta\eta|$.

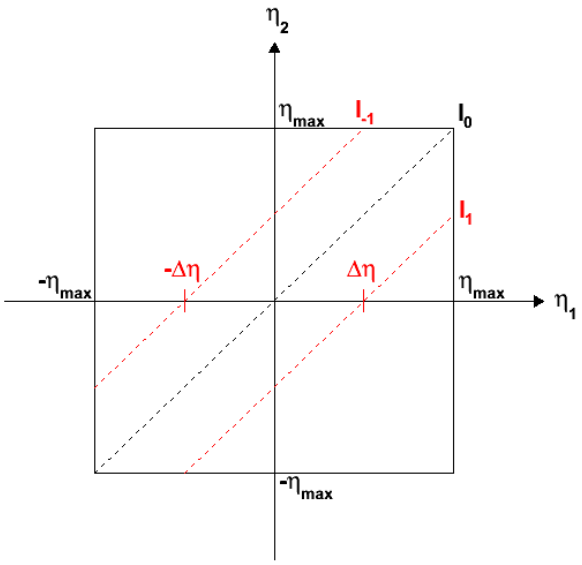

Figure 3.2: Pseudorapidity acceptance window for a pair of particles. Both particles have the same acceptance range $\eta_{1,2} \in [-\eta_{\max}, \eta_{\max}]$ which leads to a square acceptance window for the particle pair. The diagonal l_0 shows the possible (η_1, η_2) values for $\Delta\eta = 0$ and line segments l_1 and l_{-1} the possible values for some fixed $\Delta\eta > 0$ and $\Delta\eta < 0$, respectively.

The length of the hypotenuse is then given by the Pythagorean theorem:

$$L\left(l_1\right) = \sqrt{\left(\left(2\eta_{\max} - |\Delta\eta|\right)^2 + \left(2\eta_{\max} - |\Delta\eta|\right)^2\right)} = \sqrt{2}\left(2\eta_{\max} - |\Delta\eta|\right) . \tag{3.6}$$

The ratio of $L(l_0)$ and $L(l_1)$ gives the correction factor $G(\Delta\eta)$

$$\frac{1}{G(\Delta\eta)} = \frac{L(l_1)}{L(l_0)} = \frac{\sqrt{2}\left(2\eta_{\max} - |\Delta\eta|\right)}{2\sqrt{2}\eta_{\max}} = 1 - \frac{|\Delta\eta|}{2\eta_{\max}} . \tag{3.7}$$

This is normalized in such a way, that $G(0) = 1$.

3.4 Centrality selection

As discussed in Section 1.1.2, a centrality measurement is used to classify the collision geometry. The centrality of an event is defined in Eq. (1.1) to be the percentile of events, that have higher multiplicity than the event in consideration. This approach is based on an assumption, that multiplicity is a monotonic function of the impact parameter $\vec{b}$.

In the ALICE experiment the V0 amplitude distribution is used to measure the event-by-event charged particle multiplicity (see Fig. 1.4). The V0 detector is an array of scintillator detectors at forward pseudorapidity ($\eta \in [2.8, 5.1] \cup [-3.7, -1.7]$), where the signal amplitude is proportional to the number of traversing tracks.

This centrality definition can be related to the impact parameter and the collision geometry via the Glauber model. The Glauber model is a simple model for the heavy ion collisions. It treats the nucleus–nucleus collision as a multiple nucleon–nucleon collision process [60]. All these nucleon–nucleon collisions are assumed to be described by the same cross section and they are also assumed to be completely independent. The elementary nucleon–nucleon cross section is taken to be the total inelastic cross section in a proton–proton collision σ_{in}. After a single binary inelastic collision, it is assumed that a nucleon-like object emerges, that interacts basically with the same cross section with other nucleons.

Using these principles a Glauber Monte Carlo simulation is performed [14]. Then the measured multiplicity distribution is fitted based on this simulation and a few further assumptions (for details, see article [14]). From this fit the number of participants and the number of binary nucleon–nucleon collisions can be extracted. These quantities can be also calculated directly from the Glauber model as a function of the impact parameter (see Appendix C).

3.5 Measured j_T distributions

In this analysis, $\frac{1}{j_T}\frac{dN}{dj_T}$ distributions are measured. The weighting factor $\frac{1}{j_T}$ is introduced to remove the Jacobian of the polar coordinates. This can be seen by the following calculation. The vector $\vec{j_T} = (j_x, j_y)$ (see Fig. 2.2) has some distribution $f(\vec{j_T})$. In the Cartesian coordinates this is given by

$$\frac{d^2N}{dj_x dj_y} \propto f(j_x, j_y). \tag{3.8}$$

What is actually measured is the length of the vector $\vec{j_T}$. Thus the polar coordinates give a more intuitive picture of the situation. Using the transformation $dj_x dj_y = j_T dj_T d\theta$, Eq. (3.8) can be written in this new coordinate system:

$$\frac{1}{j_T}\frac{d^2N}{dj_T d\theta} \propto f(j_T, \theta). \tag{3.9}$$

It is further assumed, that $f(j_T, \theta)$ is symmetric in θ, giving $f(\vec{j_T}) = f(j_T)$. It follows that $\frac{dN}{d\theta}$ is a constant, so it can be written that

$$\frac{1}{j_T}\frac{dN}{dj_T} \propto f(j_T). \tag{3.10}$$

The $\frac{1}{j_T}$ factor can be multiplied to the other side of the equation, giving

$$\frac{dN}{dj_T} \propto j_T f(j_T). \tag{3.11}$$

If the condition $f(j_T) \to$ constant, when $j_T \to 0$ holds, Eq. (3.10) stays finite as $j_T \to 0$, but Eq. (3.11) tends to zero. This condition is found to be fulfilled in the analysis. As the signal is concentrated close to $j_T = 0$, Eq. (3.11) makes the signal difficult to see. This problem can be avoided by using the distribution in Eq. (3.10).

Tracks that fulfill the selection criteria are combined to pairs. Only the near side region is studied in this analysis, so a further condition $|\Delta\phi| < \frac{\pi}{2}$ is required from the pairs. The $\frac{1}{j_T}\frac{dN}{dj_T}$ distributions are obtained by filling the measured data into histograms in the bins of centrality, trigger particle p_T (p_{Tt}) and $k_\parallel$. The corresponding j_T and $k_\parallel$ values are calculated according to equations (2.1) and (2.2). When filling the histogram, each pair is weighted by a factor

$$w = \frac{G(\Delta\eta)C_{\text{pair}}(p_{Tt}, p_{Ta})}{j_T}, \tag{3.12}$$

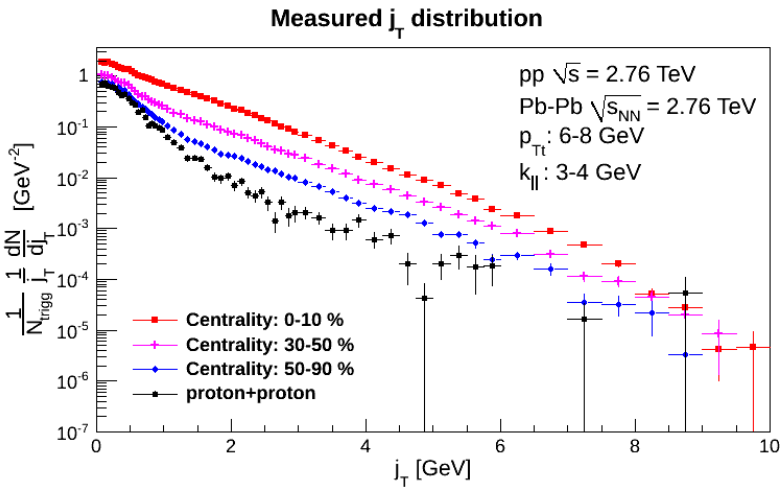

Figure 3.3: Measured j_{T} distribution for pp data at $\sqrt{s} = 2.76$ TeV (black points) and Pb–Pb data at $\sqrt{s_{\mathrm{NN}}} = 2.76$ TeV (different centrality classes marked by colored points) in $p_{\mathrm{Tt}} \in [6,8]$ GeV and $k_{\parallel} \in [3,4]$ GeV bin.

where $G(\Delta\eta)$ is the pair acceptance correction factor derived in Eq. (3.7) and $C_{\mathrm{pair}}(p_{\mathrm{Tt}}, p_{\mathrm{Ta}})$ is the pair efficiency correction factor derived in Eq. (3.5). The factor $\frac{1}{j_{\mathrm{T}}}$ is there to get the form of Eq. (3.10). The final distributions are normalized by the number of triggers and bin width. The per trigger normalization makes distributions with different number of events comparable with each other. The bin width normalization makes the distribution differential. It transforms the bin contents from being just counts to counts per unit of momentum. This gives a $\frac{\Delta N}{\Delta j_{\mathrm{T}}}$ distribution, which is usually denoted as a differential $\frac{\mathrm{d}N}{\mathrm{d}j_{\mathrm{T}}}$ distribution.

Fig. 3.3 shows an example of a measured j_{T} distribution for pp data at $\sqrt{s} = 2.76$ TeV and Pb–Pb data at $\sqrt{s_{\mathrm{NN}}} = 2.76$ TeV for several centralities in $p_{\mathrm{Tt}} \in [6,8]$ GeV and $k_{\parallel} \in [3,4]$ GeV bin. From this Figure it can be noticed, that the more central the collisions gets, the more per trigger yield there is. This is explained by the fact, that larger number of uncorrelated particles per one trigger emerge in central heavy ion collisions.

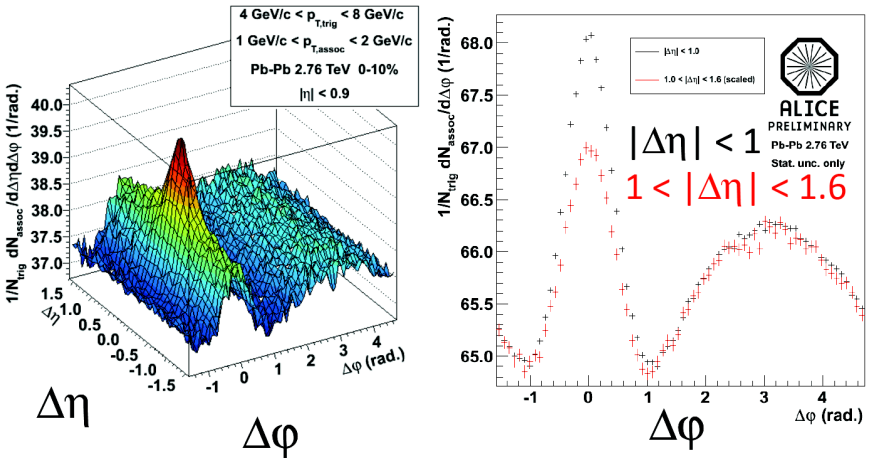

Figure 3.4: *Left:* Per trigger normalized yield of associated particles ($p_{\mathrm{Tt}} \in [4,8]$ GeV and $p_{\mathrm{Ta}} \in [1,2]$ GeV) in Pb–Pb collisions at $\sqrt{s_{\mathrm{NN}}} = 2.76$ TeV as a function of $\Delta\phi$ and $\Delta\eta$. Jet fragmentation at the near side produces a peak centered at $(\Delta\eta, \Delta\phi) = (0,0)$. *Right:* Projections of the left histogram on the $\Delta\phi$ axis in the region $|\Delta\eta| < 1$ (black) and $1 < |\Delta\eta| < 1.6$ (red). Large η swing makes the away side jet correlation structure nearly independent on $\Delta\eta$ within the limited pseudorapidity acceptance of the ALICE detector. These Figures are taken from the talk by Andreas Morsch in Hard Probes 2012.

3.6 j_T background

3.6.1 Pseudorapidity gap method

As the jets are collimated sprays of hadrons, the jet correlations are short range correlations. Hence it is expected that if a pair of particles is separated with a large pseudorapidity gap, the particles do not come from the same jet. This expectation is supported for example by the narrow near side jet peak seen in Fig. 3.4. With an assumption that the uncorrelated background comes solely from the underlying event, that is uniform in the whole phase space (good approximation for pp), the uncorrelated background can be built from large pseudorapidity gap pairs. In heavy ion collisions the collective flow causes significant long range correlations. Fortunately in the limited ALICE acceptance the flow does not seem to be dependent on pseudorapidity [17]. Thus measuring the two particle correlations for a large pseudorapidity gap is effectively a measurement of the flow [61]. Since this is uniform in pseudorapidity, the measurement can be extended to the whole pseudorapidity range. Removing this component from the data leaves only the non-flow correlations left. This method is data driven, meaning that no external parameters are needed to parametrize the flow components.

In practice, the background sampling is done in the following way:

1. Find a pair such that $|\Delta\eta| > 0.8$.
2. Generate N_{gen} new pairs such that p_{Tt}, p_{Ta}, ϕ_{t} and ϕ_{a} are kept intact but η_{t} and η_{a} are randomized according to the inclusive spectrum. The flow is preserved, since it is independent of η for constant p_{T} and ϕ.
3. Calculate $k_{\parallel}$ and j_{T} for the generated pairs.
4. Fill the background histogram weighting the results with $\frac{1}{N_{\text{gen}}}$ in addition to the regular correction factor w (Eq. (3.12)) to preserve the original number of large $\Delta\eta$ pairs.

In step 2, $N_{\text{gen}} = 20$ new pairs are generated to get better statistics for the background. The value of N_{gen} has to be relatively small so that a background where the statistical errors are much smaller than the errors originating from the fixed (p_{T}, ϕ) pairs is not generated.

The normalization for the background can be figured out using the pseudorapidity acceptance window discussed in Section 3.3. It is assumed that the particles are not from the same jet, if the pseudorapidity gap

between those is larger than some predefined value. In Fig. 3.2 this means that the background is defined to be the top left corner and the bottom right corner of the square, limited by the line segments l_1 and l_{-1}. Since all the pseudorapidity distributions are assumed to be flat, the pseudorapidity pair (η_1, η_2) appears anywhere inside the square with equal likelihood. This means that the area of a region is directly proportional to the number of particles seen in that region. The background particles are again assumed to be evenly distributed in the whole pseudorapidity range. Therefore the ratio of the area of the whole square with respect to the area of the defined background region gives the normalization factor $C_{\text{abs norm}}$

$$\frac{1}{C_{\text{abs norm}}} = \frac{A(\text{background})}{A(\text{total})} = \frac{(2\eta_{\max} - |\Delta\eta|)^2}{(2\eta_{\max})^2} = \left(1 - \frac{|\Delta\eta|}{2\eta_{\max}}\right)^2 . \tag{3.13}$$

Multiplying the particle yield in the background region with this factor gives the total background yield over the whole acceptance.

3.6.2 Radial gap method

The radial gap method is otherwise the same as the η-gap method, except that this time the background region is defined a bit differently, also $\Delta\phi$ is randomized and the normalization is different. The radial gap method can be used only in the proton–proton case, since it does not take flow into account. However, there it serves as a good comparison for the pseudorapidity gap method.

The per trigger associated yield plotted as a function of $\Delta\phi$ suggests that the region between $\Delta\phi = 0.325\pi$ rad and $\Delta\phi = 0.475\pi$ rad is mostly populated with pairs uncorrelated with the trigger in $\Delta\phi$. This assumption is backed up by the observation that the measured azimuthal correlation functions have minima at this region, see Fig. 3.5. Next it is assumed that the situation is symmetric in $(\Delta\eta, \Delta\phi)$ plane. Based on this, a circle of radius 0.325π rad is cut out from the $(\Delta\eta, \Delta\phi)$ plane to find the background. Further it is required that $|\Delta\phi| < 0.475\pi$ rad leading to a geometry shown in Fig. 3.6.

The following algorithm is used to generate the background:

1. Find a pair with $(\Delta\eta, \Delta\phi)$ value that is outside the circle but inside the rectangle in Fig. 3.6.

2. Generate N_{gen} new pairs keeping p_{Tt} and p_{Ta} fixed but sampling $\Delta\phi$ from a uniform distribution from the interval $[-\frac{\pi}{2}, \frac{\pi}{2}]$ rad and η_{t} and η_{a} from the inclusive spectrum.

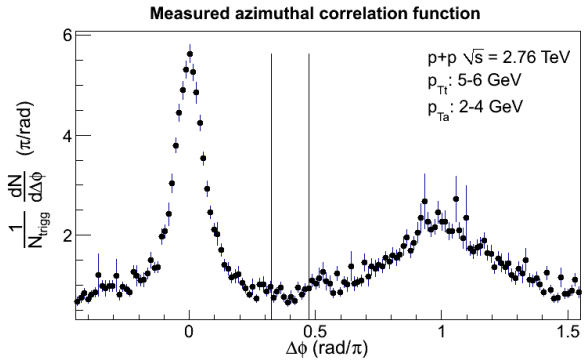

Figure 3.5: Azimuthal correlation function. The two black lines are situated at $\Delta\phi = 0.325\,\mathrm{rad}/\pi$ and $\Delta\phi = 0.475\,\mathrm{rad}/\pi$. The area between them is assumed to be populated mainly by background pairs.

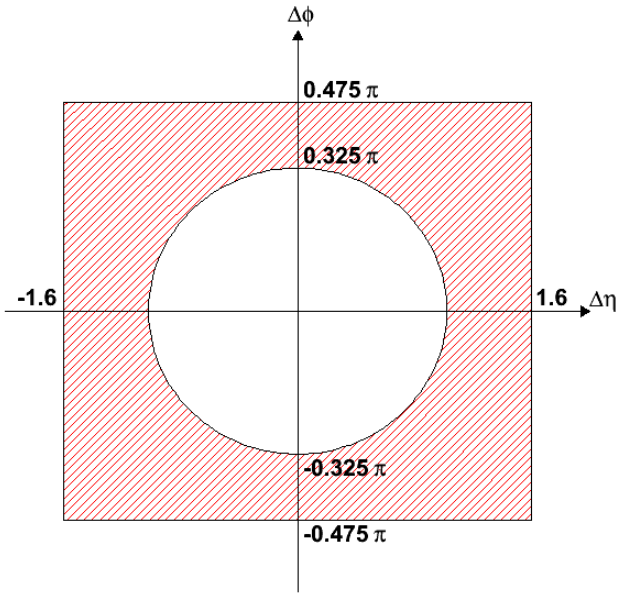

Figure 3.6: A plot showing the background region in $(\Delta\eta, \Delta\phi)$ plane in radian units. The area outside the circle but inside the rectangle that is marked with red ruling is assumed to be dominated with background pairs. The upper limits in $\Delta\eta$ direction come from the limited η acceptance.

3. Calculate $k_{||}$ and j_T for the generated pairs.

4. Fill the background histogram weighting the results with $\frac{1}{N_{gen}}$ in addition to the regular correction factor w (Eq. (3.12)) to preserve the original number of input background pairs.

The value $N_{gen} = 20$ was used in steps 2 and 4.

The normalization for this background is found by fitting it to the tail of the measured j_T distribution. It is assumed that large j_T tails of the distribution are dominated by the background contribution. This assumption is motivated by the fact that jets are quite well focused around the jet axis and big j_T values correspond to a big angle between the two particles. The normalization region boundaries are chosen to be as far as possible from the signal region. The signal to background ratio is used as a tool in this choice. Usually the start of the region is somewhere between $j_T = 3 - 4\,\text{GeV}$, depending on p_{Tt} and $k_{||}$.

This method is used to cross check the results given by the pseudorapidity gap method.

3.6.3 Background in the data

The measured j_T distribution and the estimated background components for pp data at $\sqrt{s} = 2.76\,\text{TeV}$ in $p_{Tt} \in [6,8]\,\text{GeV}$ and $k_{||} \in [3,4]\,\text{GeV}$ bin are shown in Fig. 3.7 and the measured data to background ratio for that bin in Fig. 3.8. For other bins, the measured data to background plots are presented in Appendix D. These Figures show, that the radial gap background seems to be a bit higher than the pseudorapidity gap background. This discrepancy in the background choice must be taken into account, when determining the systematic errors for the final results. The good thing is that the shapes of the two backgrounds seem to be quite similar.

The upper plot in Fig. 3.8 is a zoom to the signal region in j_T and the lower plot is a zoom to the normalization region. In the upper plot it can be seen that the data is high above the background when $j_T < 1\,\text{GeV}$. The lower plot indicates that the ratio is indeed close to 1 in higher values of j_T, which correspond mostly to the background. This gives confidence that the background determination method is consistent.

What is visible in both of the plots in Fig. 3.8 is that the error bars for radial gap are much smaller than they are for pseudorapidity gap background. This is due to higher statistics that is achieved with this

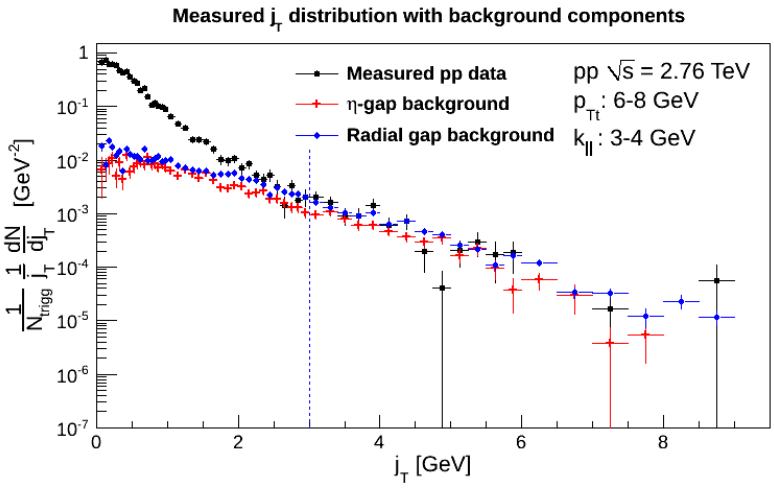

Figure 3.7: Measured j_{T} distribution (black points) and background obtained using pseudorapidity gap (red points) and radial gap (blue points) methods for pp data at $\sqrt{s} = 2.76$ TeV with $p_{\mathrm{Tt}} \in [6,8]$ GeV and $k_{||} \in [3,4]$ GeV. The blue dashed line represents the start of the normalization region for the radial gap method.

method. The price that is paid for this gain in statistics is that the method is not directly generalizable to the heavy ion case.

In Fig. 3.9 the measured Pb–Pb data can be seen with the pseudorapidity gap background and in Fig. 3.10 is the measured data to background ratio. These plots show that the measured data to background ratio is much smaller than in pp in this bin and the Figures in Appendix D confirm, that this holds for all the bins in the analysis. The immense amount of particles produced in the Pb–Pb collision explain this observation.

Because the background level is so close to the measured data, good statistics is essential for the analysis. When two numbers of similar value are subtracted from each other, a small number with a large error is left. With bad statistics, this number can fluctuate a lot.

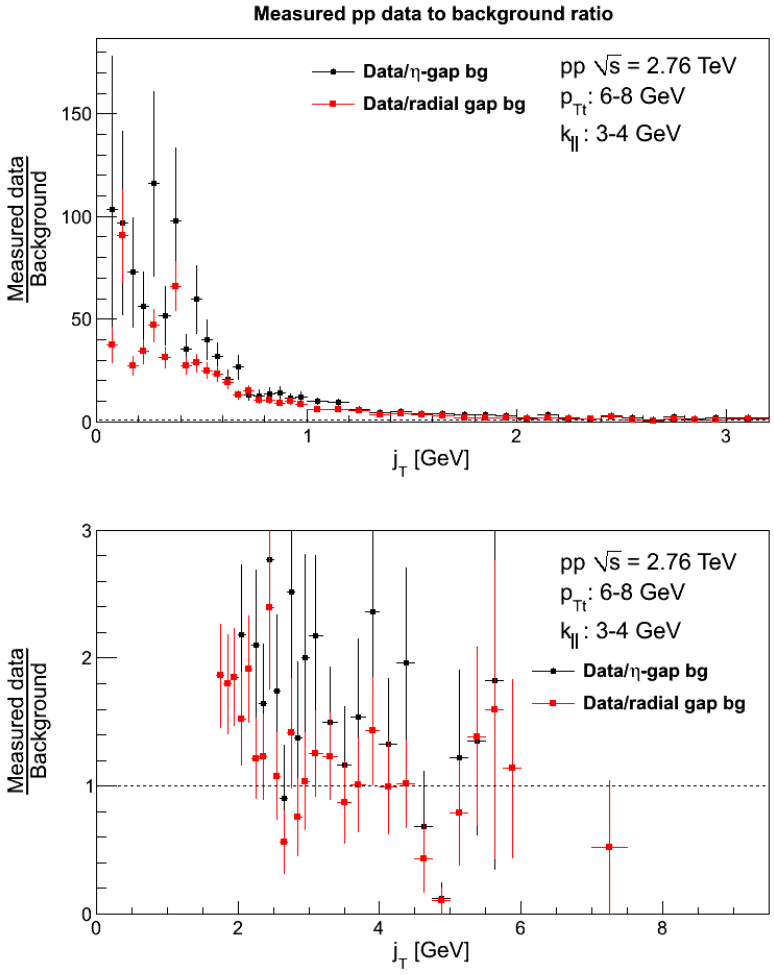

Figure 3.8: Measured data to background ratio for pp data at $\sqrt{s} = 2.76$ TeV with $p_{\mathrm{Tt}} \in [6,8]$ GeV and $k_{||} \in [3,4]$ GeV. Black points are the results for the pseudorapidity gap background and red points for the radial gap. The upper plot is a zoom to the signal region in j_{T} and the lower plot is a zoom to the normalization region.

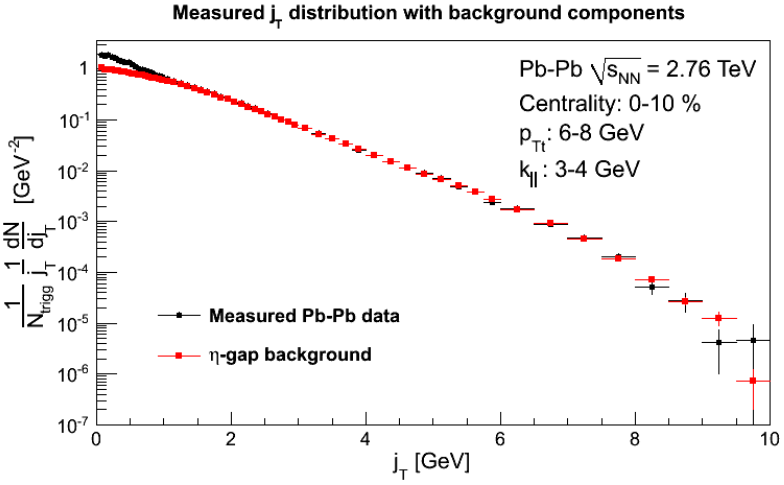

Figure 3.9: Measured data (black points) and pseudorapidity gap background (red points) for central Pb–Pb data at $\sqrt{s_{\mathrm{NN}}} = 2.76$ TeV with $p_{\mathrm{Tt}} \in [6,8]$ GeV and $k_{||} \in [3,4]$ GeV.

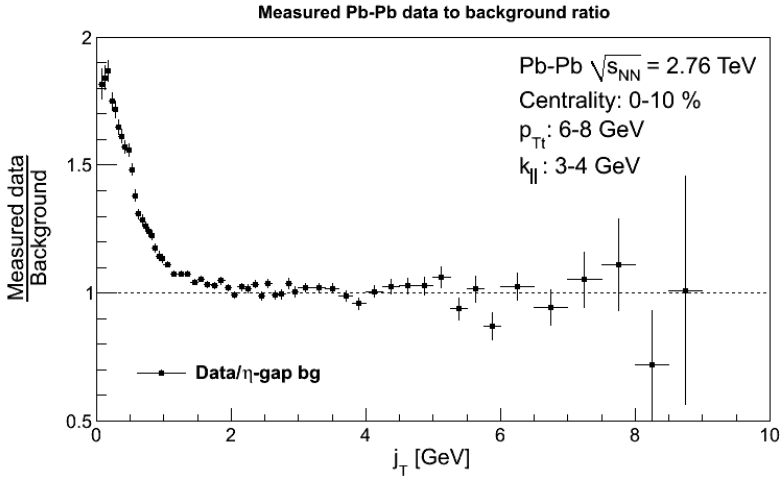

Figure 3.10: Measured data to background ratio for central Pb–Pb data at $\sqrt{s_{\mathrm{NN}}} = 2.76$ TeV with $p_{\mathrm{Tt}} \in [6,8]$ GeV and $k_{||} \in [3,4]$ GeV. The background is obtained using the pseudorapidity gap method.

Chapter 4

Results

4.1 Background subtracted j_T distributions

The j_T signals are obtained by subtracting the background histograms from the measured data histograms bin by bin. The extracted j_T signals for pp data at $\sqrt{s} = 2.76$ TeV and for different centrality classes in Pb–Pb data at $\sqrt{s_{NN}} = 2.76$ TeV are shown in Fig. 4.1. In the logarithmic scale the extracted j_T signals lie on top of each other. The small differences in signals, left after subtracting a huge background contribution, need to be studied carefully to find possible modifications in jet shapes. In the results only statistical errors are presented. Systematic errors are beyond the scope of this work.

The measured j_T data and background, the data to background ratio and the extracted signal for two different momentum bins for pp data can be found from Fig. 4.2. The same for Pb–Pb are given in Fig. 4.3. From these Figures it can be seen, that the higher the p_{Tt} and $k_{||}$ bins are studied, the more significant the signal becomes. The difference in the measured data to background ratio between the lowest and the highest bins used in the analysis is more than one order of magnitude in both pp and Pb–Pb data. This observation stems from the fact that soft physics phenomena are more important at low-p_T and jet fragmentation at high-p_T. The emergence of the jet signal is better visible in Fig. 4.3. In the left column the signal is hardly recognizable from the background but in the right column the signal stands substantially above the background.

Another thing that is noticeable in Figures 4.2 and 4.3 is the difference in the size of the error bars in low momentum bins and high momentum bins, which indicates the difference in the available statistics between these two regions.

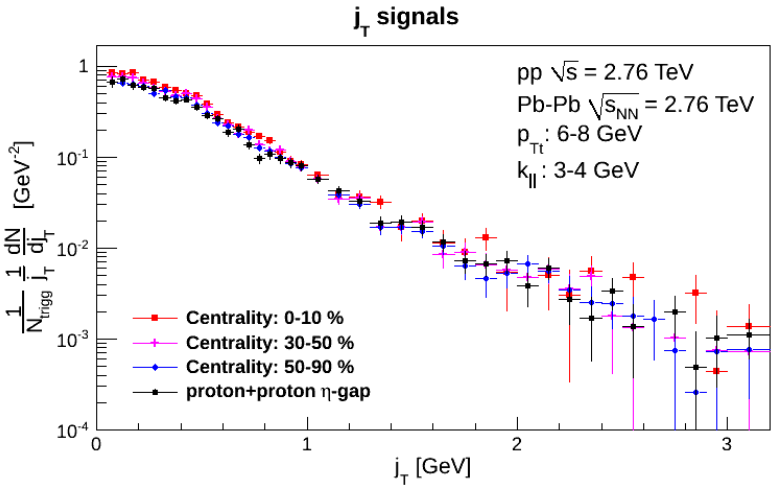

Figure 4.1: Background subtracted j_{T} distributions (signal) for $\sqrt{s} = 2.76\,\mathrm{TeV}$ data with $p_{\mathrm{Tt}} \in [6,8]\,\mathrm{GeV}$ and $k_{\parallel} \in [3,4]\,\mathrm{GeV}$. Black points are the proton–proton data and the colored points are the heavy ion data for different centrality classes. Pseudorapidity gap method is applied for all data sets to extract the signals. Only statistical errors are presented.

The situation is a trade off between the statistics and the clarity of the signal. At the small p_{T} region the statistics is good, but the signals are small. At the large p_{T} region the signals are larger, but the statistics poor.

4.2 Nuclear modifications of the j_{T} distribution

Possible signs of the medium induced modifications of the near side jet fragmentation are studied using the quantity I_{AA}, which is defined as the ratio of background subtracted j_{T} distributions in Pb–Pb and pp

$$I_{\mathrm{AA}} = \frac{\frac{1}{N^{\mathrm{AA}}_{\mathrm{trigg}}}\left(\frac{1}{j_{\mathrm{T}}}\frac{\mathrm{d}N}{\mathrm{d}j_{\mathrm{T}}}\right)_{\mathrm{AA}}}{\frac{1}{N^{\mathrm{pp}}_{\mathrm{trigg}}}\left(\frac{1}{j_{\mathrm{T}}}\frac{\mathrm{d}N}{\mathrm{d}j_{\mathrm{T}}}\right)_{\mathrm{pp}}}. \tag{4.1}$$

Taking the ratio of signals has the advantage, that it cancels out part of the systematic uncertainties and no model specific assumptions are needed for the shape of the j_{T} distributions themselves. Examples of I_{AA} distributions for different centralities are shown in Fig. 4.4.

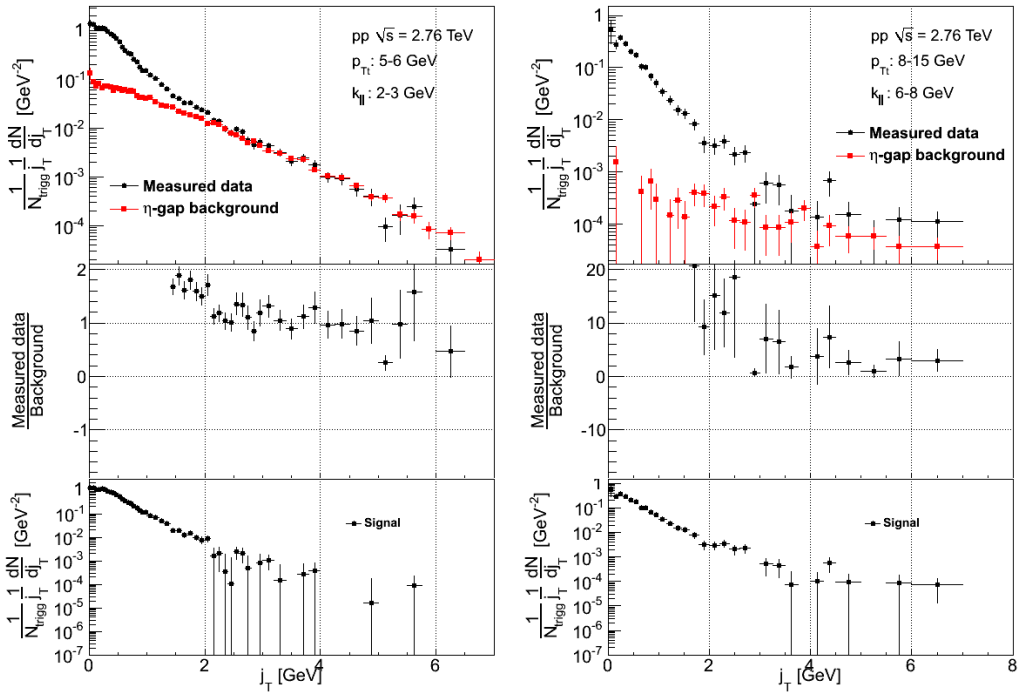

Figure 4.2: The left panel shows pp data at $\sqrt{s} = 2.76$ TeV with $p_{\mathrm{Tt}} \in [5,6]$ GeV and $k_{||} \in [2,3]$ GeV. In the right panel, there are pp data at $\sqrt{s} = 2.76$ TeV with $p_{\mathrm{Tt}} \in [8,15]$ GeV and $k_{||} \in [6,8]$ GeV. The topmost plot in both panels is the measured j_{T} distribution drawn with the pseudorapidity gap background component. The middle plot shows the measured data to background ratio zoomed close to ratio one. The extracted signals are found from the bottommost plot.

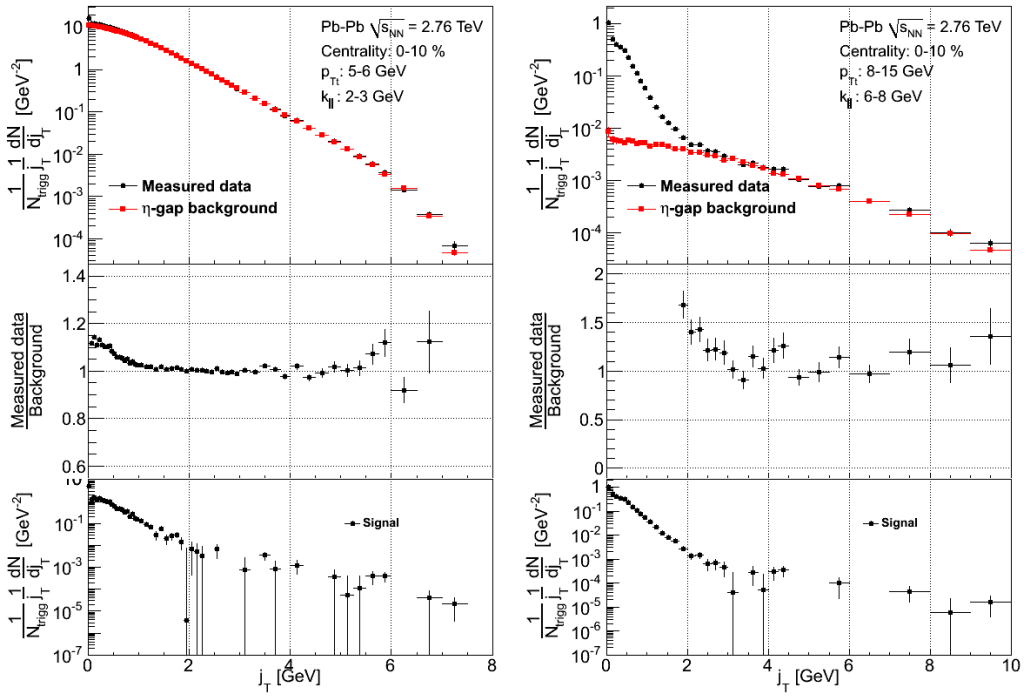

Figure 4.3: The left panel shows Pb–Pb data at $\sqrt{s_{\mathrm{NN}}} = 2.76$ TeV with $p_{\mathrm{Tt}} \in [5,6]$ GeV and $k_{||} \in [2,3]$ GeV. In the right panel, there are Pb–Pb data at $\sqrt{s_{\mathrm{NN}}} = 2.76$ TeV with $p_{\mathrm{Tt}} \in [8,15]$ GeV and $k_{||} \in [6,8]$ GeV. The topmost plot in both panels is the measured j_{T} distribution drawn with the pseudorapidity gap background component. The middle plot shows the measured data to background ratio zoomed close to ratio one. The extracted signals are found from the bottommost plot.

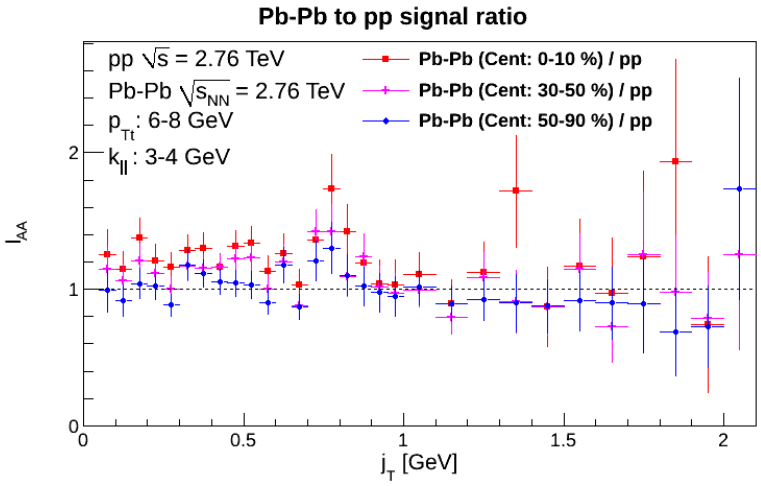

Figure 4.4: The I_{AA} ratio for $\sqrt{s} = 2.76$ TeV data with $p_{\mathrm{Tt}} \in [6,8]$ GeV and $k_{\parallel} \in [3,4]$ GeV. The color indicates the centrality class of the heavy ion signal. Figure is zoomed to the signal region in j_{T}.

The I_{AA} distributions are analyzed by studying how they evolve as a function of j_{T}. The modification of the heavy ion signal shape can be inferred from the data trend:

- rising trend = broadening
- flat trend = unmodified/scaled
- falling trend = narrowing.

This trend is investigated in this thesis by doing a linear fit to the distribution.

The region in which the fit is done is determined by studying the measured data to background figures. In all the bins used in the analysis the region $j_{\mathrm{T}} \in [0,1.5]$ GeV contains reliable signal (see Appendix D). This region also has enough data points to fit the data. When $j_{\mathrm{T}} > 1.5$ GeV, fluctuations start to play a significant role.

To see whether a first order polynomial is actually a better fit to the data than just a constant function, both of these are fitted and the χ^2 values and the number of degrees of freedom ν of the fits are extracted. A rough estimate of the goodness of fit is given by the ratio $\frac{\chi^2}{\nu}$. The closer this ratio is to one, the better description the fit gives of the data (for more information about the χ^2 test, see for example [62]).

The same procedure is done for the central and peripheral I_{AA} plots. The peripheral results are used as a reference for the central case. Since a peripheral heavy ion collision is approximately like a proton–proton collision, these ratios should always be nearly constant. So if a first order polynomial is seen to well describe data in the central case and the peripheral case is at the same time well described by a constant, this is taken as a sign of narrowing or widening of the signal.

To make a cross check, also central Pb–Pb signal to peripheral Pb–Pb signal ratio (I_{CP}) plots are made. Since peripheral collisions should approximate the proton collisions, these ratios should be close to the central I_{AA} ratios.

The I_{AA} fit results for the central data are shown in Tab. 4.1 and for the peripheral data in Tab. 4.2. All the Figures corresponding to the numerical values found from these tables are shown in Appendix D. There is a noticeable trend in the central data. A raising line seems to be the best fit for the lowest bins ($p_{\mathrm{Tt}} \lesssim 6\,\mathrm{GeV}, k_{\parallel} \lesssim 4\,\mathrm{GeV}$). From there, the description gradually changes into a constant. Again for the highest bins ($p_{\mathrm{Tt}} \gtrsim 8\,\mathrm{GeV}, k_{\parallel} \gtrsim 4\,\mathrm{GeV}$) a descending line looks like the best fit. The peripheral data looks more or less like pp data.

The widening of the signal is seen in Fig. 4.5 and the narrowing in Fig. 4.6. In these Figures the lines represent the constant and linear fits to the data sets represented by points. These fits show the difference in slopes between central and peripheral collisions while the central to peripheral data seems to be similar to central to proton–proton data.

Table 4.1: Extracted fit parameters of the constant fit and the linear fit to the central I_{AA} data. The central bin corresponds to the centrality class $0-10\,\%$.

Bin		Constant fit		Linear fit		
p_{Tt} [GeV]	$k_{\|\|}$ [GeV]	χ^2	ν	χ^2	ν	Slope
$4-5$	$2-3$	41.1	23	24.3	22	0.36 ± 0.08
$4-5$	$3-4$	43.2	23	27.1	22	0.29 ± 0.08
$5-6$	$2-3$	44.3	23	36.6	22	0.29 ± 0.11
$5-6$	$3-4$	22.0	23	20.0	22	0.13 ± 0.10
$6-8$	$2-3$	26.6	23	24.1	22	0.17 ± 0.11
$6-8$	$3-4$	22.6	23	20.2	22	-0.15 ± 0.10
$6-8$	$4-6$	17.6	23	15.6	22	-0.13 ± 0.09
$8-15$	$2-3$	22.6	23	22.6	22	-0.01 ± 0.14
$8-15$	$3-4$	40.6	23	35.4	22	-0.27 ± 0.12
$8-15$	$4-6$	59.5	23	22.1	22	-0.51 ± 0.09
$8-15$	$6-8$	18.4	11	10.4	10	-0.39 ± 0.14

Table 4.2: Extracted fit parameters of the constant fit and the linear fit to the peripheral I_{AA} data. The peripheral bin corresponds to the centrality class $50-90\,\%$.

Bin		Constant fit		Linear fit		
p_{Tt} [GeV]	$k_{\|\|}$ [GeV]	χ^2	ν	χ^2	ν	Slope
$4-5$	$2-3$	29.7	23	24.6	22	0.10 ± 0.05
$4-5$	$3-4$	13.7	23	13.4	22	0.03 ± 0.06
$5-6$	$2-3$	29.6	23	28.5	22	0.06 ± 0.06
$5-6$	$3-4$	20.7	23	20.7	22	0.01 ± 0.07
$6-8$	$2-3$	24.8	23	23.0	22	-0.09 ± 0.07
$6-8$	$3-4$	19.3	23	18.9	22	-0.05 ± 0.08
$6-8$	$4-6$	13.2	23	11.0	22	-0.12 ± 0.08
$8-15$	$2-3$	29.3	23	20.6	22	-0.24 ± 0.09
$8-15$	$3-4$	42.8	23	39.2	22	-0.17 ± 0.10
$8-15$	$4-6$	41.4	23	23.0	22	-0.32 ± 0.08
$8-15$	$6-8$	9.88	11	9.29	10	-0.10 ± 0.14

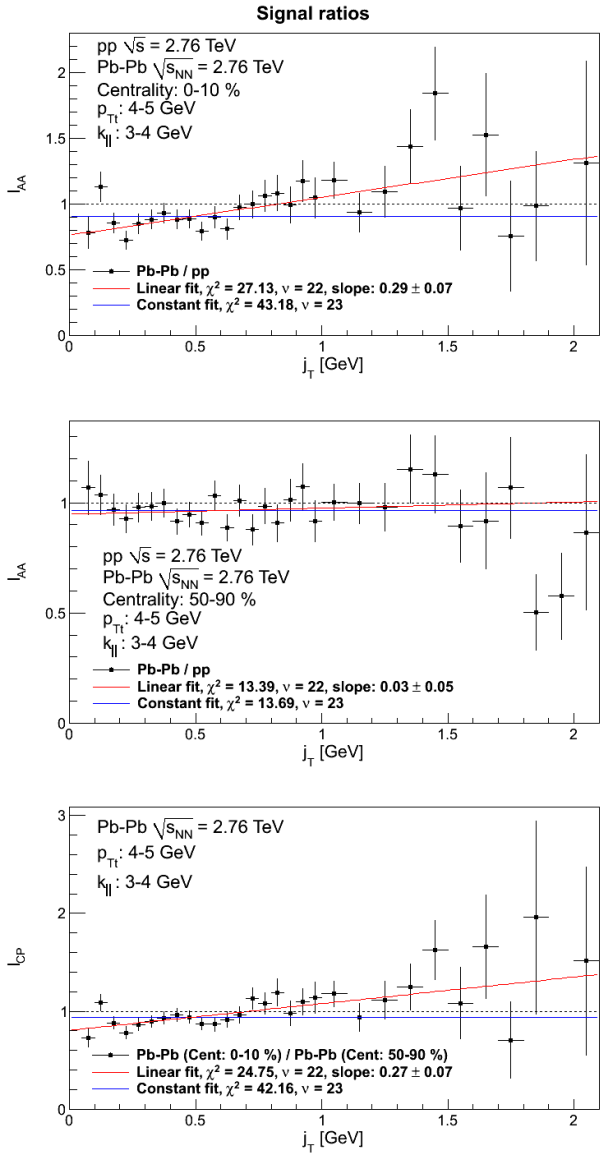

Figure 4.5: The widening of the signal peak. The uppermost plot shows the central I_{AA} ratio for $\sqrt{s} = 2.76$ TeV data with $p_{\mathrm{Tt}} \in [4,5]$ GeV and $k_{\parallel} \in [3,4]$ GeV. In the middle plot there is the peripheral I_{AA} ratio and in the bottommost plot the I_{CP} ratio for the same energy, p_{Tt} bin and $k_{\parallel}$ bin. A constant function (blue line) and a first order polynomial (red line) are fitted to all of the data sets in the interval $j_{\mathrm{T}} \in [0,1.5]$ GeV. The black dashed line marks the ratio one.

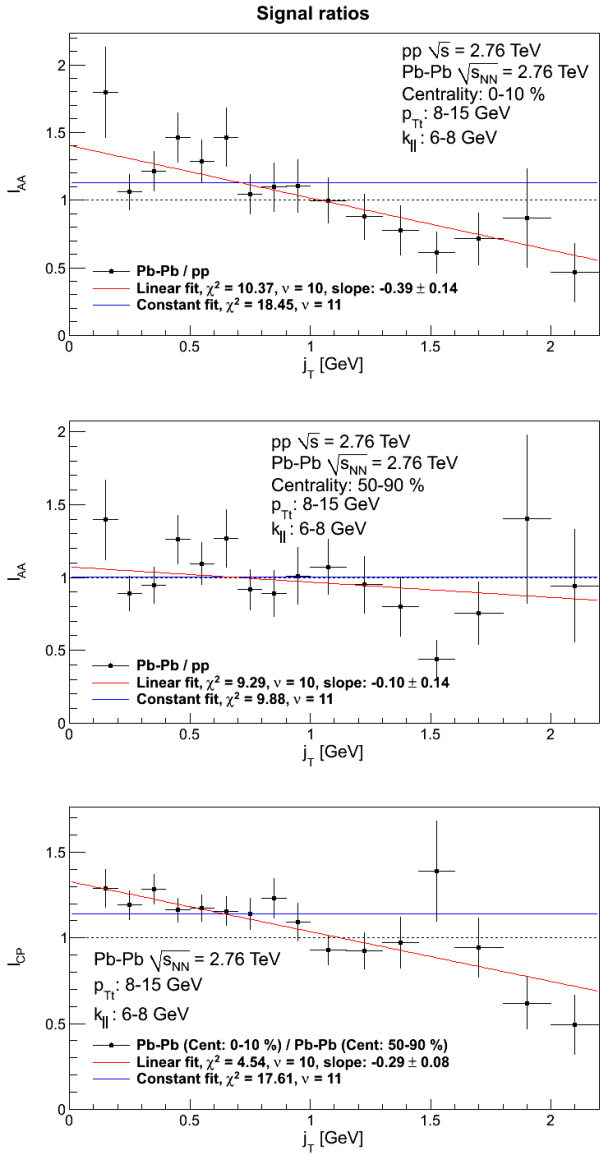

Figure 4.6: The narrowing of the signal peak. The uppermost plot shows the central I_{AA} ratio for $\sqrt{s} = 2.76$ TeV data with $p_{\mathrm{Tt}} \in [8,15]$ GeV and $k_{\parallel} \in [6,8]$ GeV. In the middle plot there is the peripheral I_{AA} ratio and in the bottommost plot the I_{CP} ratio for the same energy, p_{Tt} bin and $k_{\parallel}$ bin. A constant function (blue line) and a first order polynomial (red line) are fitted to all of the data sets in the interval $j_{\mathrm{T}} \in [0,1.5]$ GeV. The black dashed line marks the ratio one.

Chapter 5

Conclusions

The commonly used measures of energy loss in heavy ion collisions, R_{AA} and I_{AA}, were generalized in this thesis using the observable j_{T}, defined as the transverse momentum component of the jet fragment with respect to the jet axis. When the trigger particle is a leading particle with high-p_{T}, it approximates the jet axis and j_{T} can be written as the transverse momentum component of the associated particle with respect to the trigger particle (see Fig. 2.2).

The pp data at $\sqrt{s} = 2.76$ TeV and Pb–Pb data at $\sqrt{s_{\mathrm{NN}}} = 2.76$ TeV measured by the ALICE experiment were analyzed using the observable j_{T}. The modifications of transverse jet shapes in Pb–Pb compared to pp were searched by studying the ratios of the j_{T} distributions in Pb–Pb and pp collisions.

Broadening of the jet signal is seen in the low p_{Tt} and $k_{\parallel}$ region ($p_{\mathrm{Tt}} \lesssim 6$ GeV, $k_{\parallel} \lesssim 4$ GeV) and a hint of narrowing in the high p_{Tt} and $k_{\parallel}$ region ($p_{\mathrm{Tt}} \gtrsim 8$ GeV, $k_{\parallel} \gtrsim 4$ GeV). In between there is a kinematic region where no significant shape modification is observed. As discussed in Section 2.2, a possible physical scenario for the broadening would be multiple scatterings and radiative energy losses in the medium by the jet fragments together with interactions with the longitudinal flow. However, if this was the only energy loss phenomenon happening inside QGP, a broadening of the peak would be expected in all the momentum bins. Instead, the peak seems to get narrower at higher momenta. Two distinct possibilities for this are presented in Section 2.2. The first one is gluon filtering. As the medium is expected to absorb gluons more likely than quarks, the relative amount of quark jets is expected to rise. It is known that quark jets are narrower than gluon jets, so this phenomenon leads to a narrowing of the signal. The second one is a kinematic bias. The fragmentation becomes softer in medium meaning that less of the original parton momentum

is carried away by an observed hadron in the presence of medium. As harder partons have narrower fragmentation, this leads to narrower jets in the case of heavy ions as compared to pp for a fixed trigger p_{T}. The surface bias cannot explain this phenomenon, because it should make the shape of the signal in Pb–Pb approximately the same as in pp .

It is difficult to say which one of the two jet narrowing mechanisms dominates or if the narrowing is caused by some other unexpected phenomena. The shape difference caused by the fragmentation of partons with different momenta could be studied by different theory models and the results obtained from these could then be compared with the observed narrowing to estimate the contribution of the kinematic bias. If it would be possible to measure the ratio of quark and gluon jets, the effect of gluon filtering could be estimated using the ratio.

The error analysis is in progress and the systematic errors are still missing completely. The sources for systematic errors are for example the error coming form the background choice and errors in calculating different correction factors.

Appendices

Appendix A

Relativistic kinematics

To describe the experimental setup, a Cartesian coordinate system where the z-axis is aligned with the beam is used. The (x,y) plane in this system is called the transverse plane. The momentum $\vec{p} = (p_x,p_y,p_z)$ of a scattered particle is divided into two parts, transverse and longitudinal. The transverse momentum is defined as $\vec{p}_{\mathrm{T}} = (p_x,p_y)$ and the longitudinal momentum as $p_{\parallel} = p_z$. The direction of the scattered particle is described by the azimuthal angle and pseudorapidity. The azimuthal angle is the angle in the transverse plane. Pseudorapidity is defined as

$$\eta = \frac{1}{2} \ln \left(\frac{|\vec{p}| + p_{\parallel}}{|\vec{p}| - p_{\parallel}} \right) = - \ln \left(\tan \frac{\theta}{2} \right) , \tag{A.1}$$

where θ is the scattering angle in the beam direction measured with respect to the beam. A measurement of the pseudorapidity is essentially a measurement of the scattering angle. Another neat property of pseudorapidity is, that when $\frac{m}{E} \to 0$ it coincides with the regular rapidity y of the particle

$$y = \frac{1}{2} \ln \left(\frac{E + p_{\parallel}}{E - p_{\parallel}} \right) = \operatorname{artanh} \left(\frac{p_{\parallel}}{E} \right) = \operatorname{artanh} \left(v_{\parallel} \right) , \tag{A.2}$$

where $v_{\parallel}$ is the velocity of the particle in the beam direction. The terms midrapidity and forward rapidity are used to describe the scattering angle. The midrapidity is the region where $\eta \approx 0$ and $\theta \approx 90^{\circ}$ and the forward rapidity the region where $\eta \gtrsim 2$ and $\theta \lesssim 15^{\circ}$.

The scattering processes are categorized to two main classes, soft processes and hard processes, based on the square of the four-momentum that is interchanged between the scattering particles $Q^2 = (p_1 - p_3)^2$. Here

the indices 1 and 3 refer to the particles in the scattering $12 \rightarrow 34$. Q^2 is called the virtuality. Hard processes, with large Q^2, are described with perturbative QCD (pQCD) since in this case the running coupling $\alpha_s(Q^2)$ is small. It may happen in these processes that two high energy "hard" partons scatter to midrapidity. Due to confinement, they have to hadronize and form jets. On the other hand, soft processes, with low Q^2, typically cannot be described using pQCD but need phenomenological modeling. They are considered to form the so called underlying event, that has no significant correlation to jets.

Appendix B

Centrality as a fraction of total cross section

In this Appendix it is derived how to get Eq. (1.2) from Eq. (1.1) following the discussion in [60]. The probability $P(n)$ in Eq. (1.1) can be written in a different form to take into account that different impact parameters b' may produce the same multiplicity n:

$$c(N) = \sum_{n=N}^{\infty} P(n) = \sum_{n=N}^{\infty} \int_0^{\infty} \frac{2\pi b' \mathrm{d}b'}{\sigma_{\mathrm{in}}^{AB}} \rho(b')\, P(n|b')\,, \tag{B.1}$$

where $2\pi b' \mathrm{d}b'$ is the area of the ring between impact parameters b' and $b' + \mathrm{d}b'$, $\rho(b')$ is the probability of an inelastic collision at the impact parameter b' and $P(n|b')$ is the conditional probability of producing multiplicity n provided that the impact parameter is b'. Since it holds that

$$\sum_{n=1}^{\infty} P(n|b') = 1 \tag{B.2}$$

and by definition

$$\int_0^{\infty} 2\pi b' \mathrm{d}b' \rho(b') = \sigma_{\mathrm{in}}^{AB}\,, \tag{B.3}$$

Eq. (B.1) has the correct normalization $c(1) = 1$. For heavy nuclei, a continuity limit

$$\sum_{n=N}^{\infty} \to \int_N^{\infty} \mathrm{d}n = \int_0^{\infty} \mathrm{d}n \theta(n - N) \tag{B.4}$$

is a good approximation. It can also be assumed, that the function $P(n|b')$ is narrowly peaked around some average value $\bar{n}(b')$. Thus it may be

approximated that $P(n|b') = \delta(n - \bar{n}(b'))$. Applying these approximations to Eq. (B.1) gives

$$\begin{aligned} c(N) &= \int_0^\infty \mathrm{d}n\theta(n-N) \int_0^\infty \frac{2\pi b' \mathrm{d}b'}{\sigma_{\mathrm{in}}^{AB}} \rho(b')\, \delta(n - \bar{n}(b')) \\ &= \int_0^\infty \frac{2\pi b' \mathrm{d}b'}{\sigma_{\mathrm{in}}^{AB}} \rho(b')\, \theta(\bar{n}(b') - N)\,. \end{aligned} \tag{B.5}$$

Since $\bar{n}(b')$ is a monotonically decreasing function of b', it can be written that $\theta(\bar{n}(b') - N) = \theta(b(N) - b')$, where $b(N)$ is the solution of the equation $\bar{n}(b) = N$. Thus

$$\begin{aligned} c(N) &= \int_0^\infty \frac{2\pi b' \mathrm{d}b'}{\sigma_{\mathrm{in}}^{AB}} \rho(b')\, \theta(b(N) - b') \\ &= \int_0^{b(N)} \frac{2\pi b' \mathrm{d}b'}{\sigma_{\mathrm{in}}^{AB}} \rho(b') = \frac{\sigma_{\mathrm{in}}^{AB}(b(N))}{\sigma_{\mathrm{in}}^{AB}}\,, \end{aligned} \tag{B.6}$$

where $\sigma_{\mathrm{in}}^{AB}(b(N))$ is the inelastic cross section accumulated from $b' \leq b(N)$.

Appendix C

Glauber model

The Glauber model treats the nucleus–nucleus collision as a multiple nucleon–nucleon collision process [60]. All these nucleon–nucleon collisions are assumed to be described by the same cross section and they are also assumed to be completely independent. The elementary nucleon–nucleon cross section is taken to be the total inelastic cross section in a proton–proton collision σ_{in}. After a single binary inelastic collision, it is assumed that a nucleon-like object emerges, that interacts basically with the same cross section with other nucleons.

C.1 Thickness functions

A suitable formalism for calculations needs to be formed using these approximations. The discussion here is based to that in [60]. nucleon–nucleon collisions provide a starting point for the derivation. A sketch of such a process is shown in Fig. C.1 (a). The total probability to have a nucleon–nucleon collision is given by the total inelastic cross section σ_{in}. With the help of the cross section, a probability to have an inelastic nucleon–nucleon for a given impact parameter $\vec{b}$ can be written as

$$p(\vec{b}) = t(\vec{b})\sigma_{\text{in}}\,. \tag{C.1}$$

Notice that $p(\vec{b})$ is not a probability density. Eq. (C.1) defines a nucleon–nucleon thickness function $t(\vec{b})$. The thickness function takes into account the finite size of the nucleon. Since the total probability is normalized to σ_{in}, the integral of $t(\vec{b})$ over the impact parameter space is normalized to unity:

$$\int t(\vec{b})\,\mathrm{d}^2\vec{b} = 1\,. \tag{C.2}$$

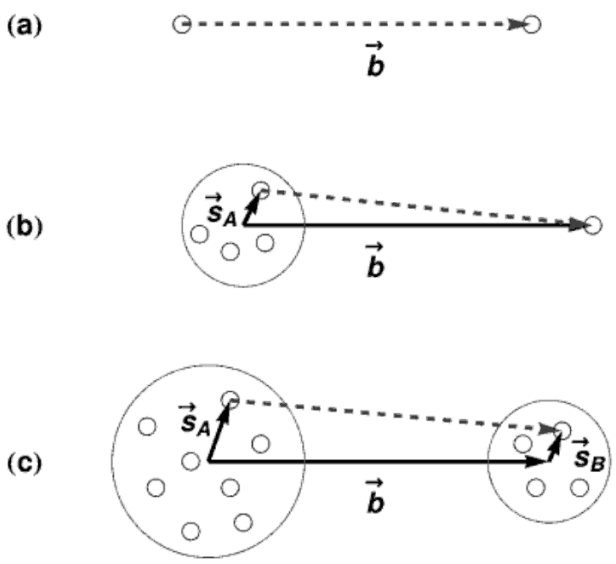

Figure C.1: A sketch of (a) a nucleon–nucleon collision, (b) a nucleon–nucleus collision and (c) a nucleus–nucleus collision in the transverse plane with respect to the collision axis. $\vec{b}$ denotes the impact parameter and the vectors $\vec{s}_A$ and $\vec{s}_B$ denote the positions of nucleons inside the nuclei A and B. Figure is taken from [60].

Before moving to consider nucleon–nucleus collisions, some kind of a description is needed for the atomic nucleus. This is an object that consists of many nucleons. Some distribution for these needs to be assumed. Woods-Saxon distribution provides quite a realistic estimate for this. The Woods-Saxon distribution for a nucleon with mass number A is of the form:

$$\rho_A(r) = \frac{\rho_0}{A\left(1+\exp\left[\frac{r-r_0}{a}\right]\right)}\,, \tag{C.3}$$

where the different parameters are given values $\rho_0 = 0.17\,\mathrm{fm}^{-3}$, $a = 0.54$ fm and $r_0 = \left(1.12\mathrm{A}^{1/3} - 0.86\mathrm{A}^{-1/3}\right)$ fm. There is one A at the denominator because this nucleon density is wanted to be interpreted as a probability distribution. This is required by the forthcoming calculations.

For simpler estimates one can use a hard sphere approximation for the nuclear density. If the nucleons are assumed to be uniformly distributed inside a hard sphere, the number density

$$\int n(r)\mathrm{d}^3r = A \;\Rightarrow\; n(r) = \frac{3A}{4\pi R^3}\,\theta(R-r)\,, \tag{C.4}$$

where R is the radius of the sphere and $\theta(x)$ is a step function, is obtained. The radius is given by the equation

$$\frac{4}{3}\pi R^3 \rho_0 = A \;\Rightarrow\; R \approx 1.12 A^{1/3}\,. \tag{C.5}$$

The ρ_0 parameter is the same as in the Woods-Saxon distribution. To be able to interpret the number density as probability density, it still needs to be normalized by the mass number:

$$\rho_A(r) = \frac{3}{4\pi R^3}\,\theta(R-r)\,. \tag{C.6}$$

Now that the nucleon distributions inside the nucleus are properly described, the nucleon–nucleus collisions can be considered. A sketch of this situation is drawn in Fig. C.1 (b). Similarly as before, a thickness function for a single nucleon–nucleon collision needs to be defined. This is called the nucleon–nucleus thickness function, or just thickness function. Now the nucleon inside the nucleus is at transverse position $\vec{s}_A$, measured from the center of the nucleus. As the impact parameter $\vec{b}$ is a vector pointing from the center of the nucleus to the incoming nucleon, the vector pointing from $\vec{s}_A$ to the incoming nucleon is $\vec{s}_A - \vec{b}$. The probability for a collision between the incoming nucleon and the nucleon at $\vec{s}_A$ is thus parametrized by the nucleon–nucleon thickness function $t(\vec{s}_A - \vec{b})$. As the nucleon inside the nucleus can be anywhere in space with a probability given by the nuclear density profile ρ_A, integration over all space is required to get an expression for the nucleon–nucleus thickness function. Collecting all this together and further assuming that the positions of the nucleons are fixed during the collision process gives:

$$T_A(\vec{b}) = \int \mathrm{d}z_A \int \mathrm{d}^2\vec{s}_A\, \rho_A\left(\sqrt{\vec{s}_A^{\,2} + z_A^2}\right)\, t(\vec{s}_A - \vec{b})\,, \tag{C.7}$$

where z_A is the coordinate along the beam. Notice that equations (C.2) and (C.3) imply the normalization

$$\int \mathrm{d}^2\vec{b}\, T_A(\vec{b}) = 1\,. \tag{C.8}$$

Similarly as before, the probability for a single nucleon–nucleon collision is now

$$p(\vec{b}) = T_A(\vec{b})\sigma_{\mathrm{in}}\,. \tag{C.9}$$

For calculations, Eq. (C.7) is a bit cumbersome, because it contains the nucleon–nucleon thickness function $t(\vec{s}_A - \vec{b})$, which is usually unknown.

To make calculations easier, it is assumed that the nucleons are point-like. In this limit, the nucleon–nucleon thickness function becomes a two-dimensional delta function. This simplifies Eq. (C.7) a lot. Making the change $t(\vec{s}_A - \vec{b}) \to \delta^{(2)}(\vec{s}_A - \vec{b})$ in Eq. (C.7) allows the integral over $\vec{s}_A$ to be done giving

$$T_A(\vec{b}) = \int \mathrm{d}z_A \, \rho_A \left(\sqrt{\vec{b}^2 + z_A^2} \right) . \tag{C.10}$$

This is just the nuclear density projected onto the transverse plane. Now the term thickness function can also be understood. In this approximation $T_A(\vec{b})$ gives the thickness of the nucleus in the transverse position $\vec{b}$.

Now only a nucleus–nucleus collision is left to be considered. Let the two colliding nucleons have mass numbers A and B. The situation is illustrated in Fig. C.1 (c). The derivation begins by finding a thickness function for a single nucleon–nucleon collision in this nucleus–nucleus collision. This is called the nucleus–nucleus thickness function, or the overlap function. Here, similar reasoning as in the case of $T_A(\vec{b})$ can be used. The nucleon at nucleus A is in the transverse position $\vec{s}_A$ and the nucleon at nucleus B is in the transverse position $\vec{s}_B$. These positions are measured from the centers of the nuclei A and B respectively. The vector pointing from $\vec{s}_A$ to $\vec{s}_B$ becomes $\vec{b} + \vec{s}_B - \vec{s}_A$. The nucleon–nucleon thickness function for these two nucleons is thus $t(\vec{b} + \vec{s}_B - \vec{s}_A)$. Both of these two nucleons can be found anywhere from space with the probability given by the nuclear density profiles. Integrating both of them over all space gives the nucleus–nucleus thickness function:

$$\begin{aligned} T_{AB}(\vec{b}) = &\int \mathrm{d}z_A \int \mathrm{d}^2\vec{s}_A \, \rho_A \left(\sqrt{\vec{s}_A^2 + z_A^2} \right) \\ &\times \int \mathrm{d}z_B \int \mathrm{d}^2\vec{s}_B \, \rho_B \left(\sqrt{\vec{s}_B^2 + z_B^2} \right) \, t(\vec{b} + \vec{s}_B - \vec{s}_A) \, . \end{aligned} \tag{C.11}$$

Above integration assumes that the positions of the nucleons are not changed in the collision. Again, notice that equations (C.2) and (C.3) imply the normalization

$$\int \mathrm{d}^2\vec{b} \, T_{AB}(\vec{b}) = 1 \, . \tag{C.12}$$

Analogously to the earlier cases, the probability for a single nucleon–nucleon collision in the nucleus–nucleus collision is given by

$$p(\vec{b}) = T_{AB}(\vec{b}) \sigma_{\mathrm{in}} \, . \tag{C.13}$$

To get rid of $t(\vec{b})$, the limit $t(\vec{b}+\vec{s}_B-\vec{s}_A) \to \delta^{(2)}(\vec{b}+\vec{s}_B-\vec{s}_A)$ is taken. Then one of the $\vec{s}$ integrals can be done with this delta function. Choosing the integral over $\vec{s}_B$ gives

$$\begin{aligned} T_{AB}(\vec{b}) &= \int \mathrm{d}^2\vec{s}_A \int \mathrm{d}z_A\, \rho_A\left(\sqrt{\vec{s}_A^2+z_A^2}\right) \int \mathrm{d}z_B\, \rho_B\left(\sqrt{\left(\vec{s}_A-\vec{b}\right)^2+z_B^2}\right) \\ &= \int \mathrm{d}^2\vec{s}_A\, T_A(\vec{s}_A)\, T_B(\vec{s}_A-\vec{b})\,. \end{aligned} \tag{C.14}$$

In this approximation it can be understood why this is called the overlap function. $T_A(\vec{s})$ represents the thickness of the nucleus at the position $\vec{s}$. Now in order for T_{AB} to be non-zero, both T_A and T_B must be non-zero at the same area in the transverse plane. So they must be overlapping.

C.2 Average number of participants and binary collisions

One of the things that can be obtained from the Glauber model is the average number of binary collisions in a heavy ion collision. For this the probability that n nucleon–nucleon collisions will happen in the nucleus–nucleus collision is needed. Take a nucleon from the nucleus A and a nucleon from the nucleus B. The probability that they will collide is $T_{AB}(\vec{b})\sigma_{\mathrm{in}}$, as given by Eq. (C.13). Since there are no other options than to collide or not to collide, the probability that they will not collide must be $1-T_{AB}(\vec{b})\sigma_{\mathrm{in}}$. As any of the A nucleons in nucleus A can collide with any of the B nucleons with nucleus B, the maximum number of binary collisions that can happen is AB. If there are n collisions happening, $AB-n$ potential collisions did not happen. The nucleons that caused the n collisions can be chosen in $\binom{AB}{n}$ ways. This reasoning gives the following expression for the probability of having n collisions:

$$P(n;A,B;\vec{b}) = \binom{AB}{n}\left[1-T_{AB}(\vec{b})\sigma_{\mathrm{in}}\right]^{AB-n}\left[T_{AB}(\vec{b})\sigma_{\mathrm{in}}\right]^{n}. \tag{C.15}$$

Now that a set of discrete numbers with a probability attached to each is obtained, the mean of this set is given by summing all the possible values together weighted by their probabilities. The average number of binary collisions is thus

$$\left\langle n(A,B;\vec{b})\right\rangle = \sum_{n=1}^{AB} nP(n;A,B;\vec{b}) = ABT_{AB}(\vec{b})\,\sigma_{\mathrm{in}}\,. \tag{C.16}$$

Notice that not much can be learned about the number of participants from this calculation. The number obtained here is much bigger than the number of participants in a collision.

Another interesting quantity given by the Glauber model in the total inelastic cross section. The total inelastic cross section corresponds to the total probability to have some kind of a collision. For this, the probabilities corresponding to different numbers of collisions need to be added up:

$$P_{\text{in}}(A,B;\vec{b}) = \sum_{n=1}^{AB} P(n;A,B;\vec{b}) = 1 - \left[1 - T_{AB}(\vec{b})\,\sigma_{\text{in}}\right]^{AB} . \tag{C.17}$$

This is the total probability to have any kind of collision at certain impact parameter $\vec{b}$. The total inelastic cross section is obtained by integrating over the impact parameter space:

$$\sigma_{\text{in}}^{AB} = \int \mathrm{d}^2\vec{b} \left(1 - \left[1 - T_{AB}(\vec{b})\,\sigma_{\text{in}}\right]^{AB}\right) . \tag{C.18}$$

Glauber model is frequently used to give an estimate for the number of participants. That is the final derivation given here. To be precise, the participants are divided into two groups. To those that may interact elastically and to those that may interact only inelastically. The latter are called wounded nucleons. The number of wounded nucleons is used to estimate the number of participants. This is a good assumption, since the elastic part of the total cross section is small compared to the inelastic part in a heavy ion collision. First it is assumed that all the nucleons in the two nuclei are at fixed positions. Consider one nucleon inside the nucleus B at transverse position $\vec{s}_i^{\,B}$. The probability for this nucleon to be wounded is needed, meaning the probability that it will collide with any of the nucleons in the nucleus A. This is obtained by calculating the probability that it does not collide with any of the nucleons and subtracting this from one:

$$p_A(\vec{s}_i^{\,B}) = 1 - \prod_{j=1}^{A} \left[1 - t(\vec{b} + \vec{s}_i^{\,B} - \vec{s}_j^{\,A})\sigma_{\text{in}}\right] . \tag{C.19}$$

Next the nucleon i in nucleus B is allowed to be anywhere it can according to the nuclear density profile. This profile is given by the thickness function T_B, which is essentially the projection of the density to the transverse plane.

Inserting this and integrating over all space gives:

$$\begin{aligned}\bar{p}(A;\vec{s}_j^{\,A};\vec{b}) &= \int \mathrm{d}^2\vec{s}^{\,B} T_B(\vec{s}^{\,B}) p_A(\vec{s}_i^{\,B}) \\ &= \int \mathrm{d}^2\vec{s}^{\,B} T_B(\vec{b}-\vec{s}^{\,B}) \left(1-\prod_{j=1}^{A}\left[1-t(\vec{s}^{\,B}-\vec{s}_j^{\,A})\sigma_{\mathrm{in}}\right]\right) \end{aligned} \quad \text{(C.20)}$$

In the above integral the following change of variables is made: $\vec{s}^{\,B} \to \vec{s}^{\,B} - \vec{b}$. Also the property $T_B(\vec{b}) = T_B(-\vec{b})$ is used. Now that the probability for a chosen nucleon to be wounded is obtained, the probability to have w_B wounded nucleons can be calculated. Using exactly the same reasoning as when calculating the number of binary collisions gives:

$$P(A;B;\vec{s}_j^{\,A};\vec{b}) = \binom{B}{w_B}\left[1-\bar{p}(A;\vec{s}_j^{\,A};\vec{b})\right]^{B-w_B}\left[\bar{p}(A;\vec{s}_j^{\,A};\vec{b})\right]^{w_B}. \quad \text{(C.21)}$$

This gives the average number of wounded nucleons in B:

$$\left\langle w_B(A;B;\vec{s}_j^{\,A};\vec{b})\right\rangle = \sum_{w_B=1}^{B} w_B P(A;B;\vec{s}_j^{\,A};\vec{b}) = B\bar{p}(A;\vec{s}_j^{\,A};\vec{b}). \quad \text{(C.22)}$$

This result still has fixed positions for the nucleons in the nucleus A. An integration over all the possible configurations is required. This is done by inserting the T_A function for every fixed nucleon:

$$\begin{aligned}\left\langle w_B(A;B;\vec{b})\right\rangle &= B\int \mathrm{d}^2\vec{s}_1^{\,A} T_A(\vec{s}_1^{\,A}) \cdots \int \mathrm{d}^2\vec{s}_A^{\,A} T_A(\vec{s}_A^{\,A}) \\ &\times \int \mathrm{d}^2\vec{s}^{\,B} T_B(\vec{b}-\vec{s}^{\,B})\left(1-\prod_{j=1}^{A}\left[1-t(\vec{s}^{\,B}-\vec{s}_j^{\,A})\sigma_{\mathrm{in}}\right]\right) \\ = B\int \mathrm{d}^2\vec{s}^{\,B} T_B(\vec{b}-\vec{s}^{\,B})&\left(1-\left[1-\int \mathrm{d}^2\vec{s}^{\,A} T_A(\vec{s}^{\,A}) t(\vec{s}^{\,B}-\vec{s}^{\,A})\sigma_{\mathrm{in}}\right]^A\right). \end{aligned} \quad \text{(C.23)}$$

This equation is obtained by noticing that actually all of the $\vec{s}_j^{\,A}$ integrals are identical and that there are A of them. To get the form that can be applied in calculations, the approximation $t(\vec{s}^{\,B}-\vec{s}^{\,A}) \to \delta^{(2)}(\vec{s}^{\,B}-\vec{s}^{\,A})$ is made to obtain:

$$\left\langle w_B(A;B;\vec{b})\right\rangle = B\int \mathrm{d}^2\vec{s}^{\,B} T_B(\vec{b}-\vec{s}^{\,B})\left(1-\left[1-T_A(\vec{s}^{\,B})\sigma_{\mathrm{in}}\right]^A\right). \quad \text{(C.24)}$$

This is the average number of wounded nucleons in the nucleus B, when it collides with A. For the nucleus A exactly the same steps can be followed. Then the total number of wounded nucleons is the sum of wounded nucleons in A and B:

$$\begin{aligned}\left\langle w(A;B;\vec{b})\right\rangle &= \left\langle w_A(A;B;\vec{b})\right\rangle + \left\langle w_B(A;B;\vec{b})\right\rangle \\ &= A\int \mathrm{d}^2\vec{s}^{\,A} T_A(\vec{b}-\vec{s}^{\,A})\left(1-\left[1-T_B(\vec{s}^{\,A})\sigma_{\mathrm{in}}\right]^B\right) \\ &+ B\int \mathrm{d}^2\vec{s}^{\,B} T_B(\vec{b}-\vec{s}^{\,B})\left(1-\left[1-T_A(\vec{s}^{\,B})\sigma_{\mathrm{in}}\right]^A\right) \quad \text{(C.25)}\end{aligned}$$

Appendix D

Figures

Hints of the jet shape modifications are sought by examining the I_{AA} (see Eq. (4.1)) plots for central Pb–Pb data. The plots for peripheral data are used as a reference. A constant function and a first order polynomial are fitted to these data sets to see if there is a rising or lowering trend in the ratio, or if the ratio is consistent with a constant. The fitting range is determined from Figures D.1–D.4. These Figures contain the measured j_{T} data to background ratio plots for pp data and central Pb–Pb data in all the p_{T} and $k_{\|}$ bins used in the analysis. All Figures are zoomed to the signal region in j_{T} to better see the signal peak. The region where the signal dies is looked for by evaluating these Figures by eye. This happens around $j_{\mathrm{T}} \sim 1.5$ GeV. Thus the fit is made in the range $j_{\mathrm{T}} \in [0,1.5]$ GeV. The I_{AA} plots for central and peripheral data for all the p_{T} and $k_{\|}$ bins with constant and linear functions fitted to them are shown in Figures D.5–D.7.

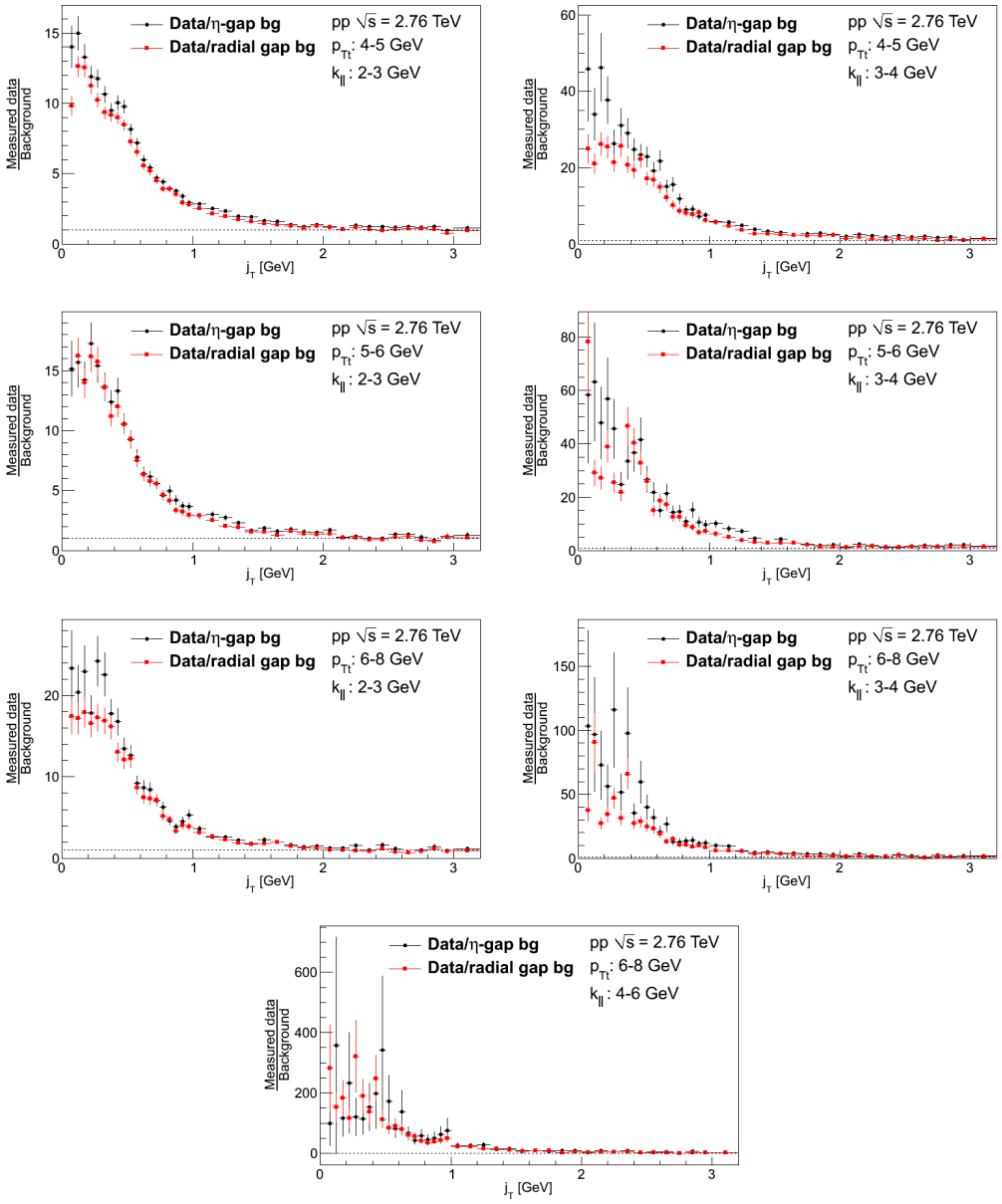

Figure D.1: Measured data to background ratio for pp data at $\sqrt{s} = 2.76$ TeV for many different p_{Tt} and $k_{||}$ bins. Black marks the results for the pseudorapidity gap background and red for the radial gap. The plots are zoomed to the signal region in j_{T}.

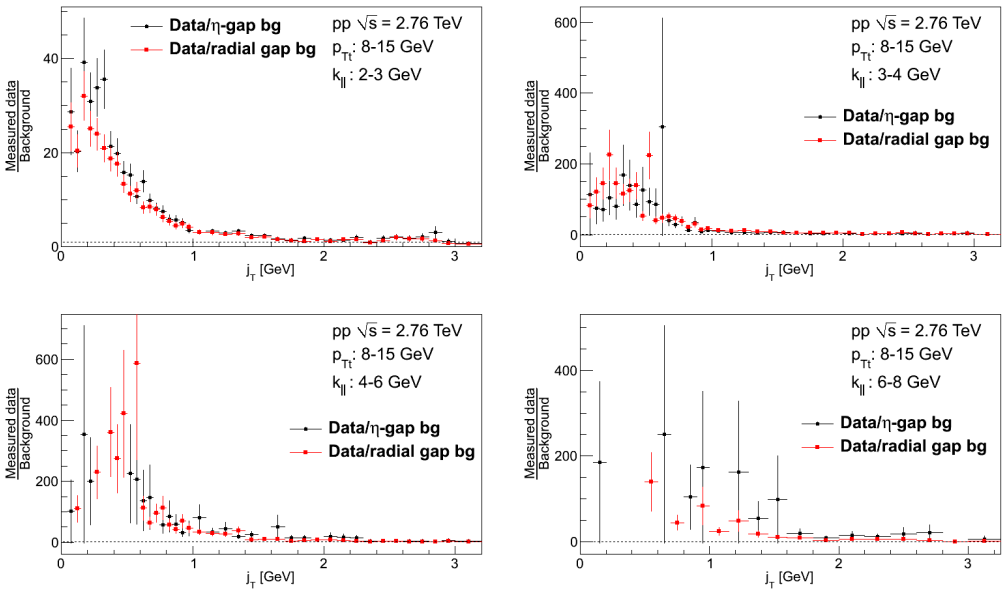

Figure D.2: Measured data to background ratio for pp data at $\sqrt{s} = 2.76$ TeV for many different p_{Tt} and $k_{||}$ bins. Black marks the results for the pseudorapidity gap background and red for the radial gap. The plots are zoomed to the signal region in j_{T}.

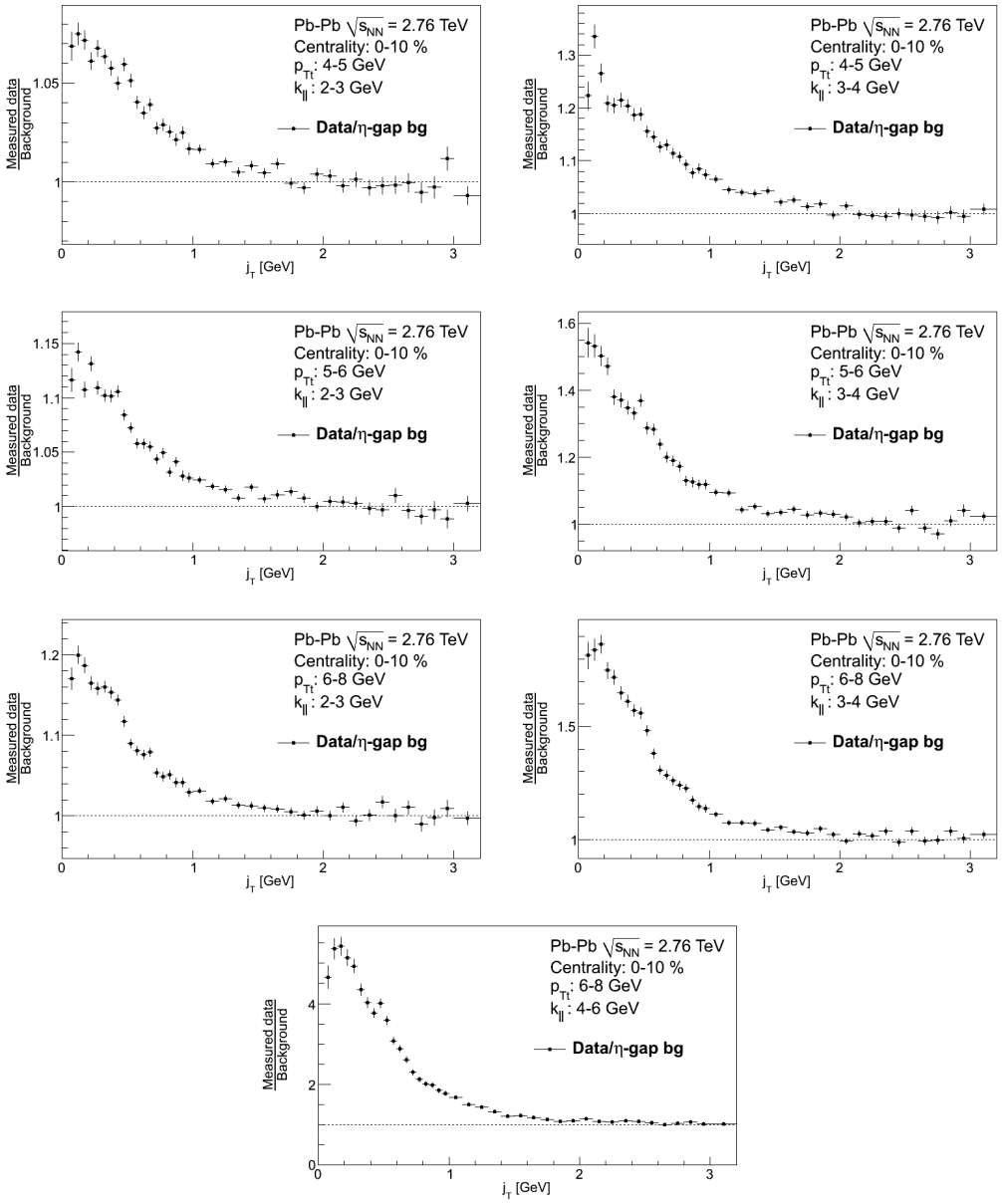

Figure D.3: Measured data to background ratio for central Pb–Pb data at $\sqrt{s_{\mathrm{NN}}} = 2.76$ TeV for many p_{Tt} and $k_{||}$ bins. The background is obtained using the pseudorapidity gap method. The plots are zoomed to the signal region in j_{T}.

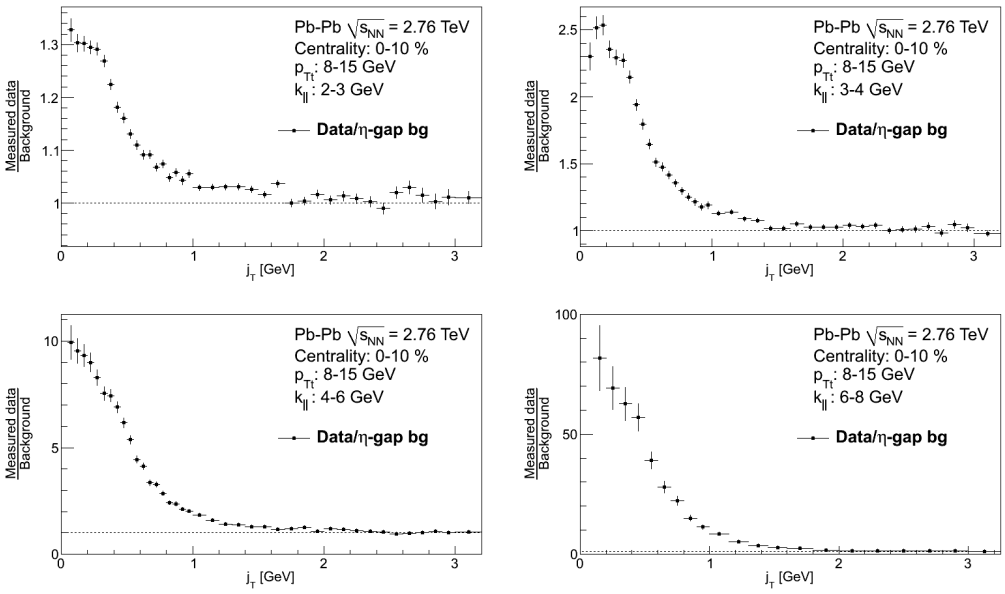

Figure D.4: Measured data to background ratio for central Pb–Pb data at $\sqrt{s_{\mathrm{NN}}} = 2.76$ TeV for many p_{Tt} and $k_{||}$ bins. The background is obtained using the pseudorapidity gap method. The plots are zoomed to the signal region in j_{T}.

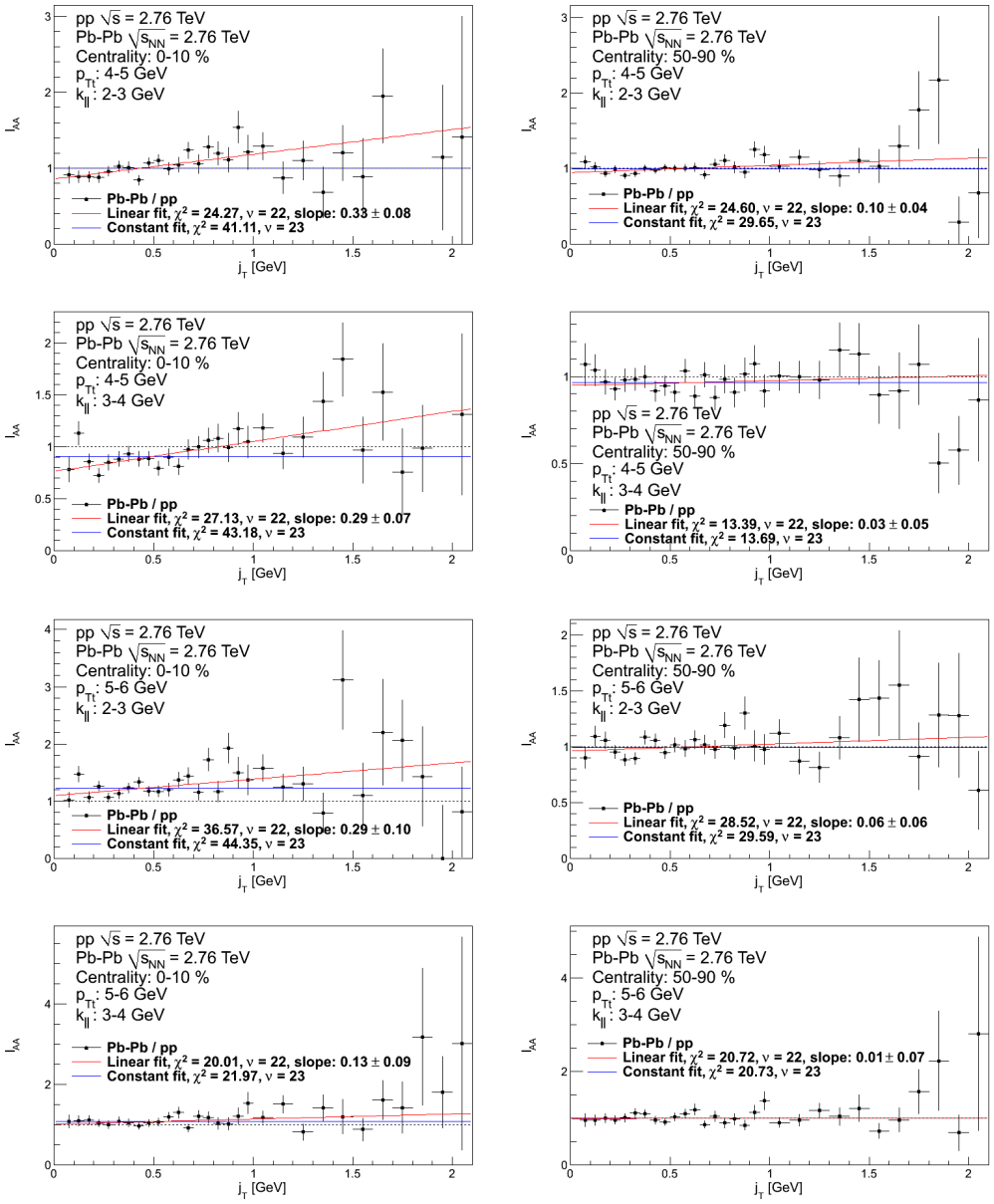

Figure D.5: Central I_{AA} ratios (left) and peripheral I_{AA} ratios (right) for $\sqrt{s} = 2.76\,\mathrm{TeV}$ data for many different p_{Tt} and $k_{||}$ bins. A constant function (blue line) and a first order polynomial (red line) are fitted to the data sets in the interval $j_{\mathrm{T}} \in [0{,}1.5]\,\mathrm{GeV}$. The black dashed line marks the ratio one.

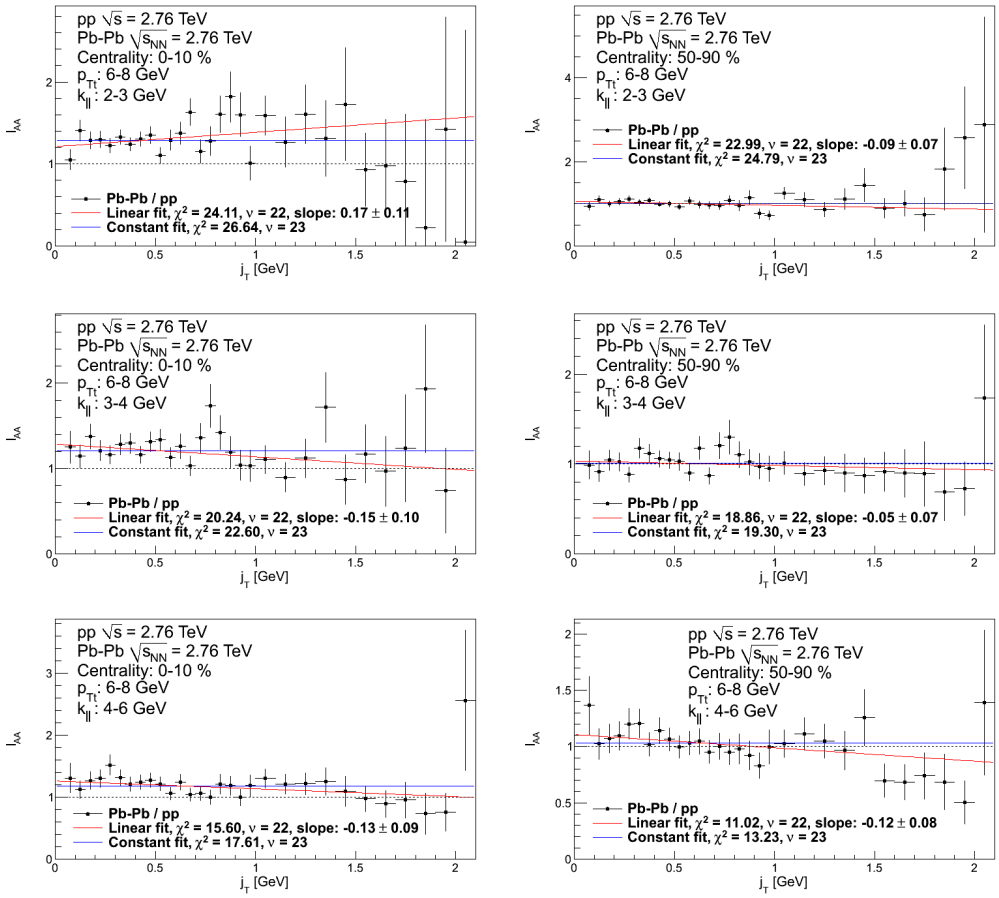

Figure D.6: Central I_{AA} ratios (left) and peripheral I_{AA} ratios (right) for $\sqrt{s} = 2.76\,\mathrm{TeV}$ data for many different p_{Tt} and $k_{||}$ bins. A constant function (blue line) and a first order polynomial (red line) are fitted to the data sets in the interval $j_{\mathrm{T}} \in [0{,}1.5]\,\mathrm{GeV}$. The black dashed line marks the ratio one.

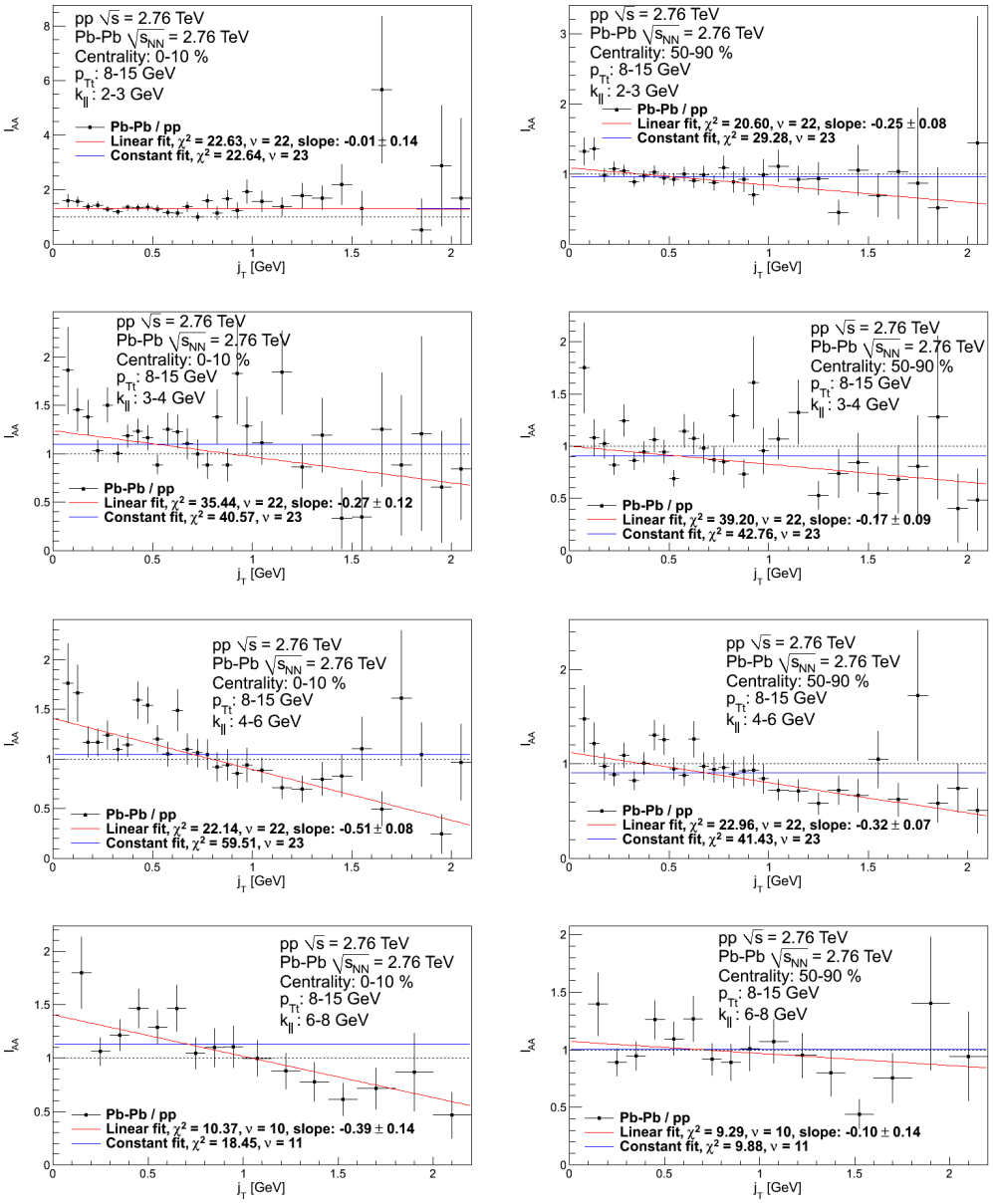

Figure D.7: Central I_{AA} ratios (left) and peripheral I_{AA} ratios (right) for $\sqrt{s} = 2.76\,\mathrm{TeV}$ data for many different p_{Tt} and $k_{||}$ bins. A constant function (blue line) and a first order polynomial (red line) are fitted to the data sets in the interval $j_{\mathrm{T}} \in [0{,}1.5]\,\mathrm{GeV}$. The black dashed line marks the ratio one.

Bibliography

[1] E. V. Shuryak, Phys.Rept. **61**, 71 (1980).

[2] J. C. Collins and M. J. Perry, Phys.Rev.Lett. **34**, 1353 (1975).

[3] M. G. Alford, A. Schmitt, K. Rajagopal, and T. Schafer, Rev.Mod.Phys. **80**, 1455 (2008), 0709.4635.

[4] D. G. d'Enterria and D. Peressounko, Eur.Phys.J. **C46**, 451 (2006), nucl-th/0503054.

[5] P. Romatschke and U. Romatschke, Phys.Rev.Lett. **99**, 172301 (2007), 0706.1522.

[6] F. Karsch, Nucl.Phys. **A590**, 367C (1995), hep-lat/9503010.

[7] J. Bjorken, Phys.Rev. **D27**, 140 (1983).

[8] F. Antinori, J.Phys.G **G38**, 124038 (2011), 1107.3957.

[9] BRAHMS Collaboration, I. Arsene *et al.*, Nucl.Phys. **A757**, 1 (2005), nucl-ex/0410020.

[10] NA49 Collaboration, T. Alber *et al.*, Phys.Rev.Lett. **75**, 3814 (1995).

[11] GSI web site: `www.gsi.de`, reference date: 12.9.2012.

[12] N. Nielsen, Am.J.Phys. **49**, 1171 (1981).

[13] R. Snellings, New J.Phys. **13**, 055008 (2011), 1102.3010.

[14] A. Toia, J.Phys.G **G38**, 124007 (2011), 1107.1973.

[15] K. J. Eskola, H. Honkanen, H. Niemi, P. Ruuskanen, and S. Räsänen, Phys.Rev. **C72**, 044904 (2005), hep-ph/0506049.

[16] M. Luzum, J.Phys.G **G38**, 124026 (2011), 1107.0592.

[17] CMS Collaboration, E. Appelt, (2011), 1110.1026.

[18] B. Andersson, G. Gustafson, G. Ingelman, and T. Sjöstrand, Phys.Rept. **97**, 31 (1983).

[19] OPAL Collaboration, P. D. Acton *et al.*, Z.Phys. **C58**, 387 (1993).

[20] C. A. Salgado and U. A. Wiedemann, Phys.Rev. **D68**, 014008 (2003), hep-ph/0302184.

[21] N. Armesto, C. A. Salgado, and U. A. Wiedemann, Phys.Rev. **D69**, 114003 (2004), hep-ph/0312106.

[22] P. B. Arnold, G. D. Moore, and L. G. Yaffe, JHEP **0206**, 030 (2002), hep-ph/0204343.

[23] S. Jeon and G. D. Moore, Phys.Rev. **C71**, 034901 (2005), hep-ph/0309332.

[24] M. Gyulassy, P. Levai, and I. Vitev, Nucl.Phys. **B594**, 371 (2001), nucl-th/0006010.

[25] S. Wicks, W. Horowitz, M. Djordjevic, and M. Gyulassy, Nucl.Phys. **A784**, 426 (2007), nucl-th/0512076.

[26] X.-N. Wang and X.-f. Guo, Nucl.Phys. **A696**, 788 (2001), hep-ph/0102230.

[27] A. Majumder, (2009), 0901.4516.

[28] T. Renk, Phys.Rev. **C78**, 034908 (2008), 0806.0305.

[29] T. Renk, Phys.Rev. **C79**, 054906 (2009), 0901.2818.

[30] J. M. Maldacena, Adv.Theor.Math.Phys. **2**, 231 (1998), hep-th/9711200.

[31] E. Witten, Adv.Theor.Math.Phys. **2**, 253 (1998), hep-th/9802150.

[32] S. Gubser, I. R. Klebanov, and A. M. Polyakov, Phys.Lett. **B428**, 105 (1998), hep-th/9802109.

[33] T. Renk and K. J. Eskola, Phys.Rev. **C75**, 054910 (2007), hep-ph/0610059.

[34] ALICE Collaboration, J. Otwinowski, Acta Phys.Polon. **B43**, 713 (2012), 1205.1655.

[35] T. Renk, Phys.Rev. **C74**, 034906 (2006), hep-ph/0607166.

[36] T. Renk, Phys.Rev. **C85**, 044903 (2012), 1112.2503.

[37] ALICE Collaboration, *Technical Design Report of the Inner Tracking System (ITS)*, 1999.

[38] ALICE Collaboration, *Technical Design Report of the Time Projection Chamber*, 2000.

[39] ALICE Collaboration, *Technical Design Report of the Transition Radiation Detector*, 2001.

[40] ALICE Collaboration, *Appendum to the Technical Design Report of the Time of Flight System (TOF)*, 2002.

[41] ALICE Collaboration, *Technical Design Report of the High Momentum Particle Identification Detector*, 1998.

[42] ALICE Collaboration, *Technical Desing Report of the Electromagnetic Calorimeter*, 2008.

[43] ALICE Collaboration, *Technical Design Report of the Photon Spectrometer (PHOS)*, 1999.

[44] E. Cuautle, A. Fernández, G. Herrera, and et al., ACORDE, The ALICE Cosmic Ray Detector, in *International Cosmic Ray Conference*, volume 5 of *International Cosmic Ray Conference*, 2008.

[45] ALICE Collaboration, *Technical Design Report on Forward Detectors: FMD, T0 and V0*, 2004.

[46] C. H. Christensen, J. J. Gaardhøje, K. Gulbrandsen, B. S. Nielsen, and C. Søgaard, Int.J.Mod.Phys. **E16**, 2432 (2007), 0712.1117.

[47] ALICE Collaboration, *Technical Design Report of the Photon Multiplicity Detector (PMD)*, 1999.

[48] ALICE Collaboration, *Technical Design Report of the Zero Degree Calorimeter (ZDC)*, 1999.

[49] ALICE Collaboration, *Technical Design Report of the Dimuon Forward Spectrometer*, 1999.

[50] M. Gyulassy, I. Vitev, X.-N. Wang, and B.-W. Zhang, Quark-gluon plasma 3 , 123 (2003), nucl-th/0302077.

[51] N. Armesto, C. A. Salgado, and U. A. Wiedemann, Phys.Rev.Lett. **93**, 242301 (2004), hep-ph/0405301.

[52] T. Renk and K. J. Eskola, Phys.Rev. **C84**, 054913 (2011), 1106.1740.

[53] CCOR Collaboration, A. Angelis *et al.*, Phys.Lett. **B97**, 163 (1980).

[54] PHENIX Collaboration, S. Adler *et al.*, Phys.Rev. **D74**, 072002 (2006), hep-ex/0605039.

[55] S. Jindariani, A. Korytov, and A. Pronko, Kt Distributions of Particles in Jets at CDF, CDF report CDF/ANAL/JET/PUBLIC/8406, 2007.

[56] ATLAS Collaboration, A. Angerami, J.Phys.G **G38**, 124085 (2011), 1108.5191.

[57] J. F. Grosse-Oetringhaus, *Measurements of Charged Particle Multiplicity in Proton-Proton Collisions with the ALICE Detector*, PhD thesis, University of Munster, 2009.

[58] ALICE Collaboration, *The ALICE Offline Bible*.

[59] F. Křížek, Private communication.

[60] W. Florkowski, *Phenomenology of Ultra-Relativistic Heavy-Ion Collisions* (World Scientific, 2010).

[61] M. Luzum, Phys.Lett. **B696**, 499 (2011), 1011.5773.

[62] J. R. Taylor, *An Introduction to Error Analysis*, 2nd ed. (University Science Books, Saulito, California, 1997).